

Stephen F. Austin State University

SFA ScholarWorks

---

Electronic Theses and Dissertations

---

6-2019

## Arachidin 3 Modulation of Lipid Metabolism in Rotavirus Infections

Stormey Wisdom

Stephen F Austin State University, wisdomsb@jacks.sfasu.edu

Follow this and additional works at: <https://scholarworks.sfasu.edu/etds>



Part of the [Biochemistry Commons](#), [Carbohydrates Commons](#), [Digestive System Diseases Commons](#), [Lipids Commons](#), [Molecular Biology Commons](#), [Other Immunology and Infectious Disease Commons](#), and the [Virus Diseases Commons](#)

[Tell us how this article helped you.](#)

---

### Repository Citation

Wisdom, Stormey, "Arachidin 3 Modulation of Lipid Metabolism in Rotavirus Infections" (2019). *Electronic Theses and Dissertations*. 243.

<https://scholarworks.sfasu.edu/etds/243>

This Thesis is brought to you for free and open access by SFA ScholarWorks. It has been accepted for inclusion in Electronic Theses and Dissertations by an authorized administrator of SFA ScholarWorks. For more information, please contact [cdsscholarworks@sfasu.edu](mailto:cdsscholarworks@sfasu.edu).

---

## Arachidin 3 Modulation of Lipid Metabolism in Rotavirus Infections

### Creative Commons License



This work is licensed under a [Creative Commons Attribution-Noncommercial-No Derivative Works 4.0 License](https://creativecommons.org/licenses/by-nc-nd/4.0/).



**Arachidin 3 Modulation of Lipid Metabolism in Rotavirus Infections**

By

Stormey Wisdom, B.S. Biochemistry

Presented to the Faculty of the Graduate School of

Stephen F. Austin State University

In Partial Fulfillment

Of the Requirements

For the Degree of

Master of Science in Biotechnology

STEPHEN F. AUSTIN STATE UNIVERSITY

August, 2019

## **Arachidin 3 Modulation of Lipid Metabolism in Rotavirus Infections**

By

Stormey Wisdom, B.S. Biochemistry

### **APPROVED:**

---

Rebecca D. Parr, Ph.D., Thesis Director

---

Odutayo Odunuga, Ph.D., Committee Member

---

Josephine Taylor, Ph.D., Committee Member

---

Donald Pratt, Ph.D., Committee Member

---

Pauline M. Sampson, Ph.D.  
Dean of Research and Graduate Studies

## **Abstract**

Rotavirus (RV) can cause severe and deadly gastroenteritis in young children, infants, and immunocompromised individuals. Previous studies have shown that arachidin 3 (A3) inhibits RV replication, and that RV replication is dependent on the presence of lipids. This study investigated the alteration of lipid metabolism by A3 in RV infected HT29.f8 cells. A decrease in the RV regulation of lipid biosynthesis genes was observed with the addition of A3 using qRT-PCR. Also, immunofluorescent and histochemical staining for neutral fats, a major component of cellular lipid droplets, revealed an increased accumulation with both RV and RV+A3 when compared to no virus and A3 controls. Furthermore, a western blot time course study of perilipin 1 presented a cycling pattern of expression with slight variations between RV, RV+A3, and A3. This data implies an association between A3 inhibition of RV replication and lipid metabolism that could be developed into a RV therapeutic treatment.

## TABLE OF CONTENTS

<b>ABSTRACT</b> .....	i
<b>TABLE OF CONTENTS</b> .....	ii
<b>LIST OF FIGURES</b> .....	iv
<b>LIST OF TABLES</b> .....	vi
<b>LIST OF ABBREVIATIONS</b> .....	vii
<b>INTRODUCTION</b> .....	1
<b>MATERIALS AND METHODS</b> .....	20
Cells and virus .....	20
RNA extraction .....	21
cDNA synthesis .....	23
Optimization of cDNA collection .....	24
Efficiency Assay .....	27
qRT-PCR .....	30
Whole cell histochemical and immunofluorescent staining .....	32
Western Blot.....	35

RT <sup>2</sup> Profiler PCR Array .....	38
<b>RESULTS</b> .....	40
Optimization of cDNA collection .....	40
Efficiency Assay .....	43
qRT-PCR .....	45
Histochemical staining .....	50
Immunofluorescent Assays .....	52
Western Blot .....	57
RT <sup>2</sup> Profiler PCR Array .....	60
<b>DISCUSSION</b> .....	66
<b>REFERENCES</b> .....	71
<b>APPENDIX</b> .....	83
<b>VITA</b> .....	87

## LIST OF FIGURES

Figure 1: RV particle structure .....	3
Figure 2: Rotavirus replication cycle .....	4
Figure 3: Arachidin 3 chemical structure .....	7
Figure 4: Cholesterol metabolism .....	13
Figure 5: Neutral fat vesicle formation .....	14
Figure 6: TEM images of RV infected HT29.f8 cells compared to treatment with A3.....	18
Figure 7: Gradient PCR assays products at 62°C, 59.1°C, 55.5°C, and 52.9°C with cDNA from Monarch® PCR & DNA Cleanup Kit from New England BioLabs® Inc. ....	41
Figure 8: GAPDH PCR Products (98 bps) using 1) unprocessed cDNA; 2) cDNA purified using Zymo One Step PCR Inhibitor Removal Kit; and 3) cDNA purified using Monarch® PCR & DNA Cleanup Kit.....	42
Figure 9: LDLR, HMGCR, PPARD, and FASN PCR assay products using unprocessed cDNA from NV and RV treatments.....	42
Figure 10: ETNK1 Expression in HT29.f8 cells at 8 hpi.....	46
Figure 11: HMGCR Expression in HT29.f8 cells at 8 hpi.....	47

Figure 12: Perilipin 4 Expression in HT29.f8 cells at 8 hpi.....	48
Figure 13: LDLR Expression in HT29.f8 cells at 8 hpi .....	49
Figure 14: Differential histochemical staining of fixed HT29.f8 cells 18 hpi using Oil Red O (red) and Hematoxylin (blue).....	51
Figure 15: Qualitative comparison of lipid droplets in RV infected and A3 treated HT29.f8 cells .....	53
Figure 16: Detection of NSP4 in RV infected cells at 8 hpi.....	55
Figure 17: Detection of NSP4 in RV infected cells at 18 hpi.....	56
Figure 18: Time course study of the expression of Perilipin 1 (PLIN1) in RV infected HT29.f8 cells treated with A3 .....	58
Figure 19: A time course study of the expression of Perilipin 1 normalized to GAPDH.....	59
Figure 20: Differential expression of key genes in lipoprotein signaling and cholesterol metabolism pathways.....	65

## LIST OF TABLES

Table 1: cDNA Mix.....	23
Table 2: Primer sets for qRT-PCR.....	28
Table 3: Thermal cycling parameters for efficiency assays .....	29
Table 4: PCR cycle conditions.....	31
Table 5: Antibodies used in western blot analysis .....	36
Table 6: PCR cycling conditions for RT <sup>2</sup> Profiler PCR Array .....	38
Table 7: Primer efficiencies calculated for lipid metabolism genes and a housekeeping gene (B2M) .....	44
Table 8: RT <sup>2</sup> Profiler PCR Array controls.....	62
Table 9: Genes that showed a >1.5 fold in up or down regulation from the RT <sup>2</sup> Profiler PCR Array .....	64
Table 10: cDNA optimization calculations .....	83
Table 11: RT <sup>2</sup> Profiler PCR Array data and calculations .....	84

## LIST OF ABBREVIATIONS

Symbol	Description
A3	Arachidin 3
ACAT	Acyl-coenzyme A:cholesterol acyltransferase
AGE	Acute Gastroenteritis
ApoB-48	Apolipoprotein B-48
BSA	Bovine Serum Albumin
CB1R	Cannabinoid receptor 1
CB2R	Cannabinoid receptor 2
cDNA	Complementary DNA
CLD	Cytoplasmic Lipid droplet
CM	Chylomicron
Ct	Threshold Cycle
DGAT	Diacylglycerol:acylCoA transferase
DLP	Double Layer Particles
DMEM	Dulbecco's Modified Eagle's Medium
DNA	Deoxyribose Nucleic Acid
dNTP	Deoxy ribonucleotide triphosphate
dsRNA	Double stranded ribonucleic acid
ECS	Endocannabinoid system

ER	Endoplasmic reticulum
FBS	Fetal bovine serum
gDNA	Genomic deoxyribonucleic acid
GI	Gastrointestinal
HMG-CoA	3-hydroxy-3-methylglutaryl-coenzyme A
HMGCR	3-hydroxy-3-methylglutaryl-coenzyme A reductase
HPI	Hours post infection
HT29	Human colon adenocarcinoma cell line
HT29.f8	Spontaneously polarizing human colon adenocarcinoma cell line
LDL	Low density lipoprotein
LDLR	Low density lipoprotein receptor
MA104	African green monkey kidney cell line
MGAT	Monoacylglycerol:acylCoA transferase
MOI	Multiplicity of infection
mRNA	Messenger ribonucleic acid
NSP	Nonstructural protein
MTTP	Microsomal triglyceride transfer protein
NV	No virus
PBS	Phosphate-buffered saline
PCR	Polymerase chain reaction
qRT-PCR	Qualitative real time polymerase chain reaction

RFU	Relative fluorescence units
RNA	Ribonucleic acid
RV	Rotavirus
RV+A3	Rotavirus with 20 $\mu$ M A3
SA11	Simian RV
SD	Standard deviation
SDS	Sodium dodecyl sulfate
SREBP	Sterol regulatory element-binding protein
TBS	Tris-buffered saline
TG	Triglyceride
TLP	Triple layered particles
VP	Viral protein
Wa	Human rotavirus strain

## INTRODUCTION

### Rotavirus

Rotavirus (RV) is classified as a member of the *Reoviridae* family of viruses that causes gastroenteritis in children under the age of 5 years and has been documented to cause severe diseases in immunocompromised individuals of all ages such as SCID, patients on chemotherapy, or transplantation patients (Annis et al., 2009; Desselberger, 2014; Lee and Ison, 2014; Liakopoulou et al., 2005; Stelzmueller et al., 2007; Sugata et al., 2012; Yin et al., 2015). According to the World Health Organization (WHO) and the Centers for Disease Control and Prevention (CDC), RV caused 577,508 deaths globally in the year 2013. (Clark et al., 2017). RV has been found to be one of the most significant pathogens associated with diarrhea cases (Alkali et al., 2015). RV infection is associated with symptoms that include watery diarrhea, severe dehydration, and fever; however, the RV infection is self-limiting, lasting only 4 – 8 days (Alkali et al., 2015). RV transmission is through the fecal-to-oral route with a 1 to 3-day incubation period which leads to the patient being asymptomatic or exhibiting acute gastroenteritis (AGE), severe diarrhea and vomiting (Bishop et al., 1973; Desselberger, 2014; Khalid et al., 2017). AGE leads to extreme dehydration which is treated with fluid balance recovery by oral hydration (Crawford et al., 2017; Khalid et al., 2017). Since the 2006 initial recommendation by the WHO to

introduce two live attenuated vaccines [RotaTeq® (Merck) and Rotarix® (GlaxoSmithKline)] in the Americas and Europe, RV cases have dramatically decreased (Abou-nader et al., 2018). However, due to the different strains of RV that infect specific regions of the world, other vaccines have been produced and used in many underdeveloped countries with additional vaccines in the pipeline of production (Bhandari et al., 2014; Crawford et al., 2017; Yen et al., 2014). Vaccines that were prequalified by the WHO in 2018, including Rotavac (Bharat Biotech International) and Rotasiil (Serum Institute of India), have also been used in clinical trial in various low-income countries (Abou-nader et al., 2018; Changotra, 2017; Deen et al., 2018; Mwila-kazimbaya et al., 2018; Plikaytis et al., 2017). China and Vietnam have locally licensed vaccines for implementation that include, respectively, LLR (Lanzhou Institute of Biological Products) and Rotavin-M1 (Center for Research and Production of Vaccines), although their clinical studies have not been performed as required by the WHO (Deen et al., 2018).

Despite the geographical strain differences in the world, RotaTeq® and Rotarix® have effectively decreased the number of RV cases and lethality of RV infections in over one hundred countries (Jiang et al., 2010). RotaTeq® includes five bovine-human reassortant strains containing the four most common VP7 serotypes and the most common VP4 serotype (Jiang et al., 2010; Vesikari et al., 2006). The Rotarix® vaccine includes a human-attenuated parental strain of RV obtained from a newborn child who experienced natural RV infection and malady

amid the 1988 – 1989 RV season (Caillot et al., 2006; Jiang et al., 2010).

Vaccines are crucial to the decrease of RV infection as well as proper and timely treatment; however, the vaccines are designed for protection against common RV strains in specific areas of the world (Jiang et al., 2010; Patton, 2009). The live virus vaccines are dependent on their genetic stability; however, it is well known that RV reassortments are common. This can result in new infectious RV strains that could ultimately affect the efficacies of the current vaccines (Patton, 2009; Weinberg et al., 2013).

The RV genome is composed of 11 segments of dsRNA that code for 6 structural (VP1, VP2, VP3, VP4, VP6, and VP7) and 6 non-structural proteins (NSP1, NSP2, NSP3, NSP4, NSP5, NSP6) (Mcclain et al., 2010).

A RV virion is characterized as a triple-layer particle (TLP) which is made up of a

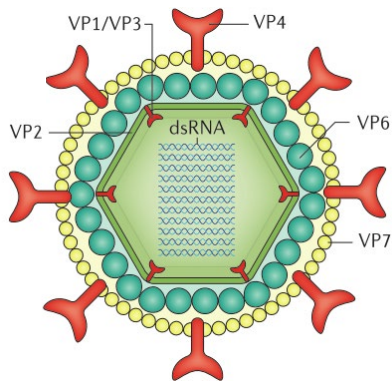
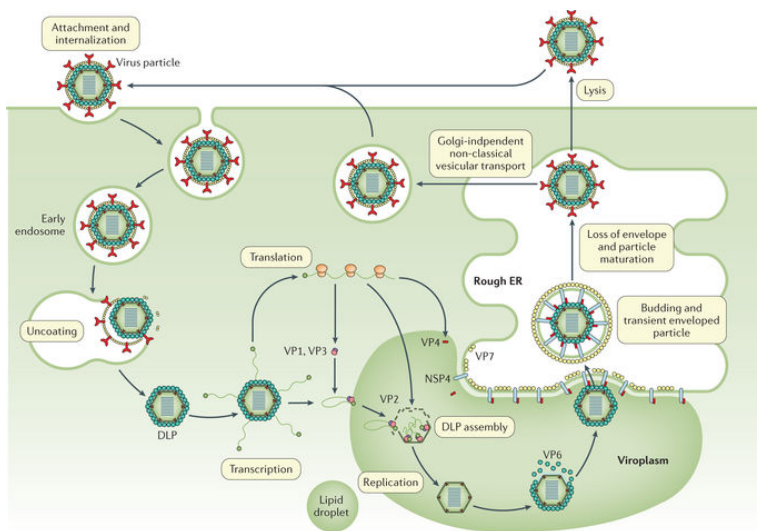


Figure 1. RV particle structure (Sue E. Crawford et al. 2017)

VP2 core shell, a middle VP6 layer and an outer VP7 layer which is implanted with VP4 spike attachment proteins as depicted in Figure 1 (Li et al., 2009; Settembre et al., 2011). Enclosed in the VP2 core shell is the dsRNA viral genome with the RNA dependent RNA polymerase and a complex made up of VP1 polymerase and VP3 RNA

capping enzyme (Desselberger, 2014; Prasad et al., 1996). VP1 polymerase is required to be bound by VP2 to initiate genome replication (Lu et al., 2009). The intermediate capsid layer is composed of the viral protein, VP6, which binds to

VP2 and stabilizes the very fragile core of the capsid (Trask et al., 2012). VP6 is also crucial for attachment and entry into a host cell due to its service as an adaptor for the RV outer capsid proteins, VP4 and VP7 (Trask et al., 2012). The most abundant viral protein, VP7, is located on the outer smooth layer of the capsid (Khodabandehloo et al., 2012). VP7 is dependent on two calcium ions being bound at each subunit interface for stability as it forms a continuous, perforated shell on top of VP6 (Aoki et al., 2010; Trask et al., 2012). Embedded into the VP7 layer are 60 trimeric spikes that are formed by the viral attachment protein, VP4 (Trask et al., 2012). Viral attachment is dependent on VP4; however, before the virion can bind to the host and enter the cell, VP4 must be cleaved by trypsin-like proteases into VP5 and VP8 (Crawford et al., 2017, 2001; Trask et al., 2012). After the uptake of the virus by the cell, low calcium levels within the endosome induce the removal of VP7 and VP4, releasing the



transcriptionally active double-layered particle (DLP) into the cytoplasm as shown in Figure 2 (Trask et al., 2012).

The understanding of RV entry and vesicular

traffic has been a slow

Figure 2. RV replication cycle (Sue E. Crawford et al. 2017)

and challenging process due to the inability to manipulate the genome of the

virus (Arias et al., 2015). Located on the inner surface of the VP2 layer, the RV particle possesses its own transcription complex (TC) (Desselberger, 2014; Jayaram et al., 2004). The TC consists of VP1, the viral RNA-dependent RNA polymerase, VP3 and a dedicated viral RNA segment (Desselberger, 2014; Jayaram et al., 2004). Within the DLP, VP1 initiates the negative strand of genomic RNA to produce capped, non-polyadenylated, (+) ssRNA transcripts (Desselberger, 2014; Ruiz et al., 2009). Upon the release of the transcripts from the DLP, they can serve either for translation into viral proteins or as templates for replication to create the dsRNA genomes of RV progeny as outlined in figure 2 (Desselberger, 2014; Silvestri et al., 2004). Within the cellular cytoplasm, RV DLPs are transcriptionally active and produce large amounts of mRNAs provided there is a sufficient supply of energy (ATP) (Cohen et al., 1979; Desselberger, 2014; Lawton et al., 1997; Lu et al., 2008; Spencer and Arias, 1981). Before replication of the templates can begin, a viroplasm must form and this is achieved with the use of a ubiquitous cellular kinase, CK1 $\alpha$  (Criglar et al., 2018). In addition to the viral properties of NSP2, it also has several enzymatic activities which include nucleoside-triphosphatase (NTPase), which allowing NSP2 to autophosphorylate at multiple sites (dNSP2). This leads to the association of NSP5 that has been hypophosphorylated by CK1 $\alpha$  (Criglar et al., 2018). The dNSP2-NSP5 complex is then phosphorylated again by CK1 $\alpha$  which triggers the relocation for viroplasm formation (Criglar et al., 2018). The trafficking of the complex to the location of viroplasm formation converts dNSP2 to vNSP2,

representing the form of NSP2 exclusively located on the viroplasm resulting in the necessary curvature for viroplasm assembly (Criglar et al., 2018). Next, repeated rapid hyperphosphorylation of NSP5 by CK1 $\alpha$  leads to the growth and maturation of the viroplasm (Criglar et al., 2018). At this time the viroplasm is formed around the transcriptionally active DLPs (Trask et al., 2012). Within the viroplasms, early virion assembly occurs by selected (+)ssRNAs being assembled into VP2 cores and replicated by VP1 into the dsRNA genome (Trask et al., 2012). The particle therefore expands and the VP6 layer is acquired forming a 100 nm sized particle; however, prior to the completion of DLP assembly NSP2 must be removed (Li et al., 2009; Long and McDonald, 2017; Ruiz et al., 2009). The addition of VP4 and VP7 occurs in the endoplasmic reticulum (ER) once the developing DLPs egress from the viroplasms to convert the DLPs to TLPs, restoring the RV particles' full infectivity (Lopez et al., 2005). NSP4 participates in this process as an intercellular receptor by interacting with VP6 (Desselberger, 2014). RV TLPs are then released in a budding process that is not immediately fatal for the cell or well understood (Desselberger, 2014).

### Arachidin 3

Peanuts (*Arachis hypogaea*) produce a defense against infections around sites of wounding by upregulating the production of stilbene derivatives (Sobolev, 2013). In the peanut plant, prenylated stilbenoids are naturally produced as phytoalexins, which include an isopentenyl moiety (3-methyl-1-butenyl) such as

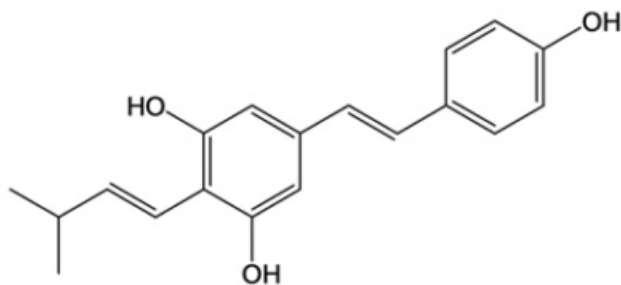


Figure 3. Arachidin 3 chemical structure (Yang et al., 2016)

A3 (Figure 3) (Bennett and Wallsgrove, 1994; Roupe et al., 2006; Yang et al., 2016).

Stilbenoids are phenolic compounds derived from the phenylpropanoid/acetate

pathway (Huang et al., 2010; Moss et al., 2013). Among the stilbenoid compounds, resveratrol has become the most studied stilbenoid due to its anti-inflammatory and antioxidant properties along with antitumor, antibacterial and antiviral effects (Aggarwal et al., 2004; Athar et al., 2009; Ball et al., 2015; Roupe et al., 2006). However, due to limited oral bioavailability and rapid absorption and metabolism, the potential human usage is restricted. (Gambini et al., 2015; Tomé-Carneiro et al., 2013; Yang et al., 2016).

It has been shown that prenylated resveratrol analogs, such as A3, have increased lipophilicity allowing for easier interaction with cell membranes, enhancing access and association with potential membrane-bound molecular targets responsible for beneficial biological activity (Brents et al., 2012; Huang et

al., 2010). Furthermore, A3 has been demonstrated to bind to both cannabinoid receptor 1 (CB1R) and cannabinoid receptor 2 (CB2R) while acting as a competitive antagonist of CBR1 and agonist of CB2R (Brents et al., 2012). Due to the increased bioavailability and potential cell signaling, the use of A3 could initiate a protective effect against RV infections.

### **Cannabinoid Receptors**

The endocannabinoid system (ECS) is an important lipid signaling and immunomodulator system that is highly conserved dating back to at least 600 million years (Acharya et al., 2017; McPartland et al., 2006; Sharma et al., 2015). The ECS is found throughout the body in the central nervous system as well as in peripheral tissues and the gastrointestinal (GI) tract (Pacher and George, 2013; Wright et al., 2005). Within the GI tract, the ECS is an important regulatory system, working in control of food intake, nausea, and intestinal inflammation (Izzo and Camilleri, 2008). The ECS is composed of cannabinoid receptors (CBRs), endocannabinoids, and enzymes, with the two main receptors being cannabinoid receptor 1 (CB1R) and cannabinoid receptor 2 (CB2R) (Troy-Fioramonti et al., 2015).

In 1988, a G-protein coupled protein receptor that bound to cannabinoids was discovered in rat brain tissue; subsequently, in 1990 this receptor was cloned and renamed CB1R (Devane et al., 1988; Matsuda et al., 1990). In 1993, CB2R was identified in macrophages (Munro et al., 1993; Rodriguez De Fonseca and

Schneider, 2008). CB1R is mainly expressed in the central and peripheral nervous system, including the enteric nervous system; however, CB2R is found in immune cells (Trautmann and Sharkey, 2015). CB2R serves an important role in immune function and inflammation but it also serves a role in reducing visceral sensitivity and regulating abnormal accelerated motility (Di Marzo and Izzo, 2006; Sharkey and Wiley, 2016). The receptors have also been found in the gastrointestinal (GI) tract and have shown to be important in the regulation of immune homeostasis, GI motility and secretion (Acharya et al., 2017; Hasenoehrl et al., 2016). CB1R has been determined to be involved in the function of relaxation of the lower esophageal sphincter and inhibition of gastric acid secretion (Wright et al., 2008).

In the presence of pathologically increased intestinal motility elicited by an inflammatory stimulus, CB1R and CB2R are both activated in the gut (Pacher et al., 2006). It has been shown that A3 is a competitive CB1R antagonist as well as having significant affinity binding to CB2R suggesting that A3 acts as a novel ligand at CBRs (Brents et al., 2012).

### **Lipid Metabolism**

Viruses depend on host metabolism to supply the high amounts of energy required for viral replication (Plaza et al., 2016). The sequestering of energy from the host cell is performed by altering metabolic processes that are critical for the survival of the cell to the benefit of virus replication but detrimental for the host

(Plaza et al., 2016; Sanchez and Lagunoff, 2015). One of the metabolic processes altered is lipid biosynthesis which affect lipid signalling pathways, stored cellular lipid, and influences lipid trafficking (Mazzon and Mercer, 2014). Of the many mechanisms exploited during viral infections, cholesterol synthesis and the storage of esterified sterols and neutral fats are the most commonly affected (Fernández De Castro et al., 2016).

### *Cholesterol Metabolism*

Cholesterol serves multiple functions in the human body as it is a critical part of cell membranes and functions as a precursor for bile acids, steroid hormones, and vitamin D (Reeskamp et al., 2018). Cholesterol metabolism is tightly regulated, with a major role for the liver and intestines (Kriaa et al., 2019; Reeskamp et al., 2018). Enterocytes in the intestinal tract are unique from other cells in the human body as they have three sources of cholesterol while other cell types have only two sources (Engelking et al., 2012). Similar to other cells, enterocytes source cholesterol by endogenous synthesis of sterol *de novo* and the uptake of LDL (low density lipoproteins)-derived cholesterol from the plasma; however, enterocytes are distinct from other cells in that they also absorb free cholesterol from the gut lumen (Degirolamo et al., 2015; Engelking et al., 2012; Silva Afonso et al., 2018). Intracellular cholesterol levels are modulated by a negative feedback loop in which *de novo* cholesterol synthesis and LDL cholesterol uptake are tightly regulated by an endoplasmic reticulum (ER) membrane bound transcription factor, sterol regulatory element-binding protein

(SREBP), which prevents cholesterol overload in the cell (Alphonse and Jones, 2016; Asano et al., 2017; Degirolamo et al., 2015; Goldstein and Brown, 2009).

The cholesterol biosynthetic pathway is a complex biochemical process that occurs in the ER and requires more than 30 chemical reactions (Alphonse and Jones, 2016; Silva Afonso et al., 2018). The rate limiting step of *de novo cholesterol synthesis* is the reaction of membrane-bound enzyme 3-hydroxy-3-methylglutaryl-coenzyme A reductase (HMGR) converting 3-hydroxy-3-methylglutaryl-coenzyme A (HMG-CoA) to mevalonate (Voet and Voet, 2011).



In cholesterol depleted cells, SREBPs are transported to the Golgi complex to be processed by two proteases that release a soluble fragment of SREBP. This fragment enters the nucleus where it activates the transcription of genes encoding HMGR and all other enzymes involved in cholesterol biosynthesis. A previous study's analysis of the effects of lovastatin, a HMGR inhibitor, on SA11 (Simian RV) infected MA104 (African green monkey kidney cell line) cells revealed that when HMGR is inhibited, both cholesterol levels and RV titers are reduced (Mohan et al., 2008). Also the effects on shows defective, "empty-looking" virus particles inside the cell (Mohan et al., 2008). This study indicates the importance of *de novo* cholesterol biosynthesis in the infection and assembly of RV particles; however, this study was performed using SA11 and MA104 cells

rather than the human RV strain (Wa) and a human intestinal cell line (Mohan et al., 2008).

At the same time that the genes encoding HMGCR and all other enzymes involved in cholesterol biosynthesis are activated, the gene encoding LDL receptor is also activated (Goldstein and Brown, 2009). As LDL-derived cholesterol begins entering the cell, it blocks the transport of SREBPs to the Golgi complex, thereby transcription of all the target genes decline and the cell produces less cholesterol (Goldstein and Brown, 2009). LDL receptors (LDLR) are found on the cell surface where they bind to LDL particles with high affinity. Once a LDL particle binds to the LDLR forming a LDLR-LDL particle complex it is endocytosed into coated vesicles (Silva Afonso et al., 2018). The vesicles will then fuse to form endosomes with a low internal pH causing the LDLR to release the LDL particle and return to the cell surface (Silva Afonso et al., 2018). The LDL particle is then incorporated into lysosomes where it is degraded resulting in cholesteryl esters (Silva Afonso et al., 2018). The cholesteryl esters are hydrolyzed and remain in the cell, whereas free cholesterol can be re-esterified by acyl-coenzyme A:cholesterol acyltransferase (ACAT) in the ER and either stored in lipids droplets in the cytoplasm or chylomicrons for export out of the cell (Degirolamo et al., 2015; Silva Afonso et al., 2018) (Figure 4).

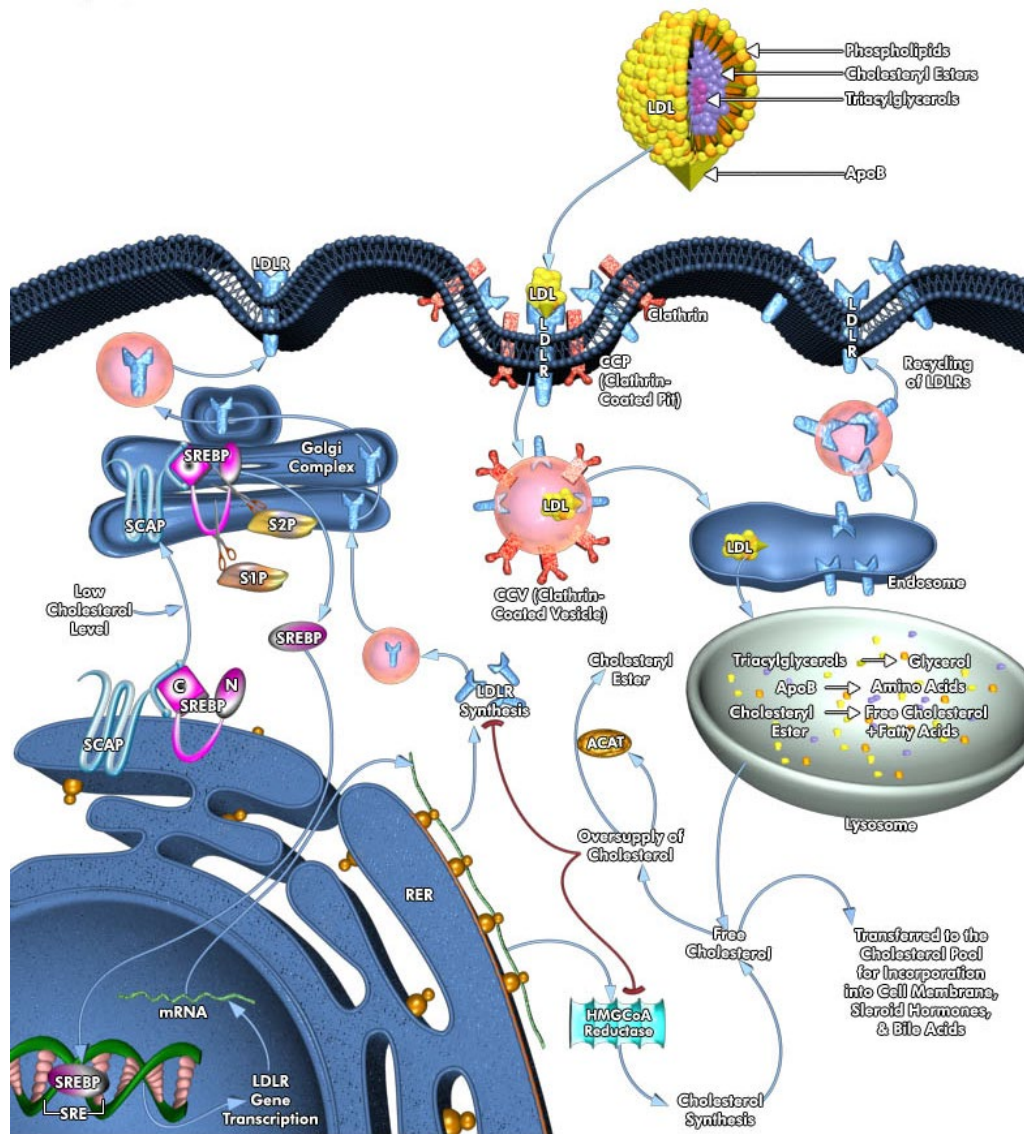


Figure 4. Cholesterol metabolism (© 2009 QIAGEN, all rights reserved)

### Neutral Fat Vesicles

The lipids synthesized in the ER can either become part of a cytosolic lipid droplet or a chylomicron for secretion. Fatty acids that have been endocytosed by enterocytes are metabolized by the monoacylglycerol pathway.

Monoacylglycerol: acylCoA transferase (MGAT) converts fatty acids into

diacylglycerol, which is then converted to triglycerides (TG) by diacylglycerol acylCoA transferase (DGAT). The newly synthesized TGs accumulate between the two leaflets of the ER phospholipid membrane (Beilstein et al., 2016). The nascent lipid droplet will then either bud into the ER lumen or into the cytosol; however the mechanism that controls the budding of the nascent lipid droplet is still unclear (Beilstein et al., 2016) (Figure 5).

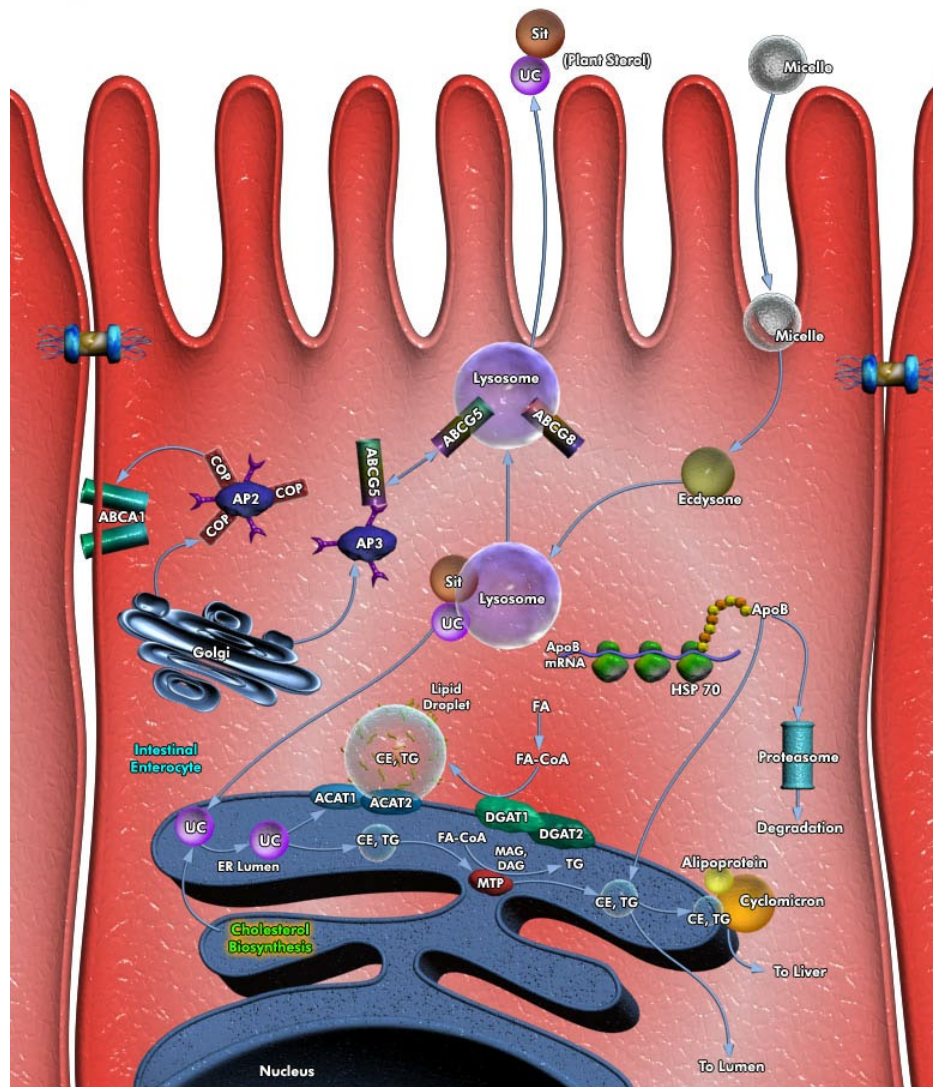


Figure 5. Neutral fat vesicle formation (© 2009 QIAGEN, all rights reserved)

In most cells the nascent lipid droplet will bud towards the cytoplasm, however in cells that assemble lipoproteins such as enterocytes, they may partition towards the ER lumen to form a chylomicron (CM) (Hussain, 2009). As TGs are accumulating in the ER membrane, apolipoprotein B-48 (ApoB-48) is being assembled to form a complex with the nascent lipid droplet (Auclair et al., 2017). ApoB-48 is a structural protein that facilitates the formation of the CM within the ER with the assistance of a microsomal triglyceride transfer protein (MTTP) (Auclair et al., 2017). The pre-CM vesicle is then transported to the Golgi complex with the assistance of Sar1B GTPase (Auclair et al., 2017; Demignot et al., 2013). This initiates the vesicular coat protein complex II-dependent transport for trafficking through the ER-Golgi secretory compartments where it ultimately buds out of the cell, entering the blood stream (Auclair et al., 2017; Demignot et al., 2013). The function of the CM is for transportation of lipids to other organs (Demignot et al., 2013).

If the nascent lipid droplet buds into the cytosol, perilipins, a multi-protein family (5 members), targets the surface of a lipid droplet and regulates lipid storage and hydrolysis (Beilstein et al., 2016). Cytosolic lipid droplets (CLD) are composed of a hydrophobic TG and cholesteryl ester core (neutral fats) surrounded by a phospholipid monolayer with very few cholesterols and proteins (Auclair et al., 2017). The function of the CLD is for mobilization and storage of neutral fats that are utilized in various ways including nutrient storage, cytoplasmic chaperones for toxic proteins and lipids, and as signaling platforms

for immune response pathways (Henne et al., 2018). Interestingly, a study by Heller and colleagues suggests an immunoregulation within the inflammatory pathway that affects lipogenesis, with the accumulation of fats in lipid droplets occurring in intestinal cell lines, HT29 and NCM460 (Auclair et al., 2017; Heller et al., 2016). RV infection is known to cause inflammation in the intestines (Holloway and Coulson, 2013). Because the viral phosphoprotein, NSP5, is inserted on the surface of the viroplasm in a similar pattern as the phosphoprotein, perilipin A, on CLDs, their potential relationship was examined (Cheung et al., 2010). Confocal microscopy and fluorescence resonance energy transfer (FRET) experiments were employed to show RV-induced viroplasms physically interacts with CLD-associated proteins (perilipin A and ADRP) and lipids (Cheung et al., 2010). Also, the treatment of RV-infected cells with either triacsin C compound, which blocks CLD formation, or the combined treatment of isoproterenol and IBMX, which induces fragmentation of CLDs into smaller microdroplets, produces a 4-fold decrease in viral RNA replication with a 100-fold significant decrease of infectious viral progeny (Cheung et al., 2010). This suggests viral replication and the production of infectious virus particles is dependent of the production of CLD vesicles and is sensitive to the fragmentation of CLDs into microdroplets. Additionally, RV-infected cells with both treatments exhibited a higher viability compared to untreated control cells at 21 hpi and 16 hpi, respectively (Cheung et al., 2010). However, the triacsin C treatment resulted in a distinct decrease in the number of cells containing viroplasms and

the number of viroplasms/cell (Cheung et al., 2010). This alteration in the viroplasms of infected cells is not found with the combined treatment of isoproterenol and IBMX; which indicates an association of lipids with functional viroplasms where new immature virus particles are assembled (Cheung et al., 2010). To further investigate the role of lipids in RV infections, de novo cholesterol biosynthesis and fatty acid synthesis were inhibited with the addition of lovastatin and the combination of TOFA (5- (tetradecyloxy)-2-furoic acid) and the compound C75 (tetrahydro-4-methylene-2R-octyl-5-oxo-3S-furancarboxylic acid), respectively (Gaunt et al., 2013; Mohan et al., 2008). The RV RNA and protein production remains unchanged; however, the RV progeny displays a decrease in infectivity (Gaunt et al., 2013; Mohan et al., 2008). Additionally, transmission electron microscopy (TEM) shows that lovastatin treated RV-infected cells, results in the accumulation of defective, “empty-looking” virus particles (Mohan et al., 2008). These results infer that lipids are essential for the efficient production and assembly of infectious virus particles. However, the underlying mechanism of action remains to be fully understood (Lever and Desselberger, 2016).

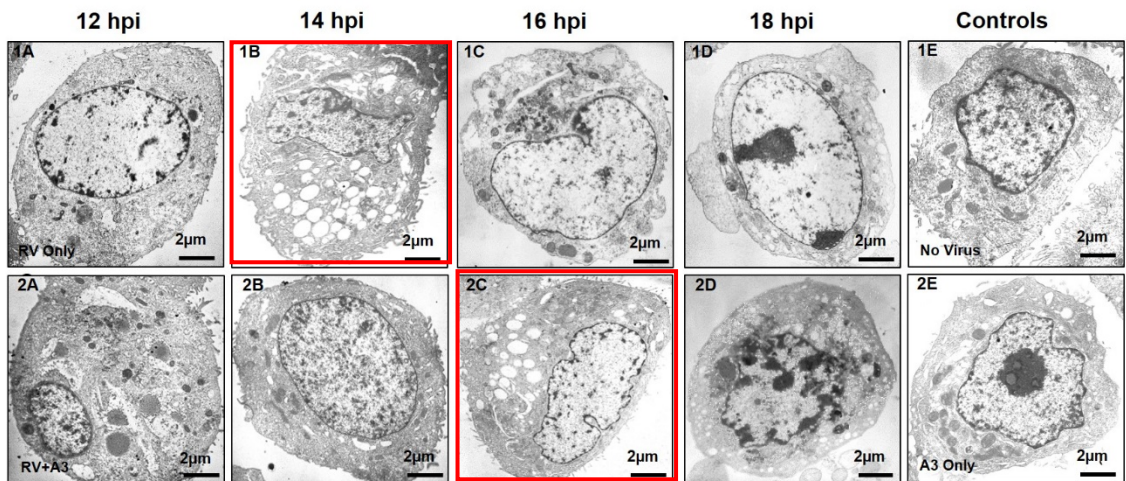


*Figure 6. TEM images of RV infected HT29.f8 cells compared to treatment with A3. Panels 1A-1D are RV only infected HT29.f8 cells. Panels 2A – 2D are RV+A3. Panel 1E is NV control and panel 2E is A3 only control (Witcher 2017)*

The Parr laboratory used transmission electron microscopy (TEM) to show RV infected HT29.f8 cells treated with A3 exhibited a two-hour delay in lipid vesicle formation compared to RV only, from 14 hours post infection (hpi) to 16 hpi (Figure 6 1B and 2C). Correspondingly, microarray analysis results revealed regulation of 4 genes (AGPAT4, ETNK1, MSMO1, and PRKAB2) in lipid biosynthesis, indicating that lipid metabolism appears to be a significant factor in RV infections (Lockwood, 2017). Therefore, this research project studied the regulation of lipid metabolism in RV infected cells and in RV infected cells treated with A3.

Our hypothesis is that the up-regulation of lipid metabolism by RV in HT29.f8 cells is moderated with the addition of A3 to restore lipid homeostasis. The hypothesis is supported by the TEM images showing lipid vesicle formation being affected within RV-infected cells as well as a decrease in the production of

infectious RV particles with the addition of A3 (Lockwood, 2017; Witcher, 2017). This suggests that A3 could be used as a potential therapeutic agent for RV infection. This hypothesis was tested by comparing RV infected HT29.f8 cells to RV infected cells treated with A3 using the following 4 techniques: (1) qRT-PCR was used to compare mRNA levels of the 4 previously reported genes (AGPAT4, ETNK1, MSMO1, and PRKAB2) and an addition 5 genes (FASN, HMGCR, PPARD, LDLR, and Perilipin 4) that were shown in the literature to encode for regulatory enzymes in lipid metabolic pathways (Voet and Voet, 2011); (2) Visualized the distribution and accumulation of neutral fats using immunohistochemical and immunofluorescent assays; (3) Illustrated the effects of RV infections and A3 treatments on PLIN1 protein using western blot analysis; and (4) Compared metabolic profiles for lipoprotein and cholesterol metabolism between RV infected and A3 treated cells using a RT<sup>2</sup> Profiler PCR array.

## **Materials and Methods**

### **Cell line and virus**

The human colon adenocarcinoma cell line HT29.f8, a clonal cell line derived from the parent cell line (HT29) were grown in Dulbecco's Modified Eagle's Medium (DMEM) supplemented with 10% fetal bovine serum (FBS), 2 mM L-glutamine, and 20 U/mL Penicillin/Streptomycin at 37°C with 5.0% CO<sub>2</sub>. The human RV strain, Wa, was acquired from Dr. Judith M. Ball, Texas A&M University. HT29.f8 cells were grown to 80% confluency and then infected with Wa RV strain at a multiplicity of infection (MOI) of 2 as previously described (Ball et al., 2015) . Briefly, the medium was replaced at 12 hours prior to an infection with DMEM without FBS to synchronize the cell cycle to G<sub>0</sub> for an efficient RV-infection as shown in previous experiments (Arnold et al., 2012; Ball et al., 2015). Cells were infected with virus in the presence of 10µg/ml of Worthington trypsin (Biochemical Corporation, Lakewood, NJ) for one hour at 37°C in 5% CO<sub>2</sub> with rocking. Media was changed and incubated in DMEM without FBS with trypsin at 0.1 µg/ml for 8 hours at 37°C in 5% CO<sub>2</sub> as described previously (Ball et al., 2015).

## **RNA extraction**

At 8 hpi the Zymo Research Quick-RNA MiniPrep kit (Zymo Research Irvine, CA) was used for total RNA extraction and purification. The media was removed from the cells and lysis buffer was added to the sample. The amount of lysis buffer used was 300  $\mu\text{L}$  for  $1 \times 10^6$  cells. The lysed cells were transferred to labeled 1.5 mL RNase-free microfuge tubes and passed through a clean RNase-free 26G<sup>3/8</sup> syringe 5 – 10 times each to shear the DNA making the solution less viscous and easier to isolate RNA. The samples were then centrifuged at 12,000  $\times g$  for 1 minute to clear lysate. The supernatant was transferred into a labeled spin-away filter (yellow) in a collection tube and centrifuged at 12,000  $\times g$  for 1 minute to remove gDNA. The flow-through was saved for RNA purification.

Ethanol (95-100%) was added in 1 volume (300  $\mu\text{L}$ : 300  $\mu\text{L}$ ) to the sample in RNA lysis buffer and mixed well. A volume of 600  $\mu\text{L}$  of the mixture was transferred to a Zymo-Spin™ IIICG column (green) in a collection tube and centrifuged for 30 seconds. The column was then washed with the addition of 400  $\mu\text{L}$  of RNA wash buffer and centrifuged for 30 seconds discarding the flow-through. For each sample, DNase I reaction mix was prepared by combining 5  $\mu\text{L}$  of DNase I and 75  $\mu\text{L}$  of DNA digestion buffer in a RNase-free tube and mixed well by gentle inversion. The 80  $\mu\text{L}$  of DNase I reaction mix was then added directly to the column matrix and incubated at room temperature for 15 minutes then centrifuged for 30 seconds. The RNA Prep Buffer (400  $\mu\text{L}$ ) was added to each column and centrifuged for 30 seconds. The column was then washed with

the addition of 700  $\mu\text{L}$  of RNA wash buffer and centrifuged for 30 seconds. The column was washed a final time with 400  $\mu\text{L}$  of RNA wash buffer and centrifuged for 2 minutes to ensure the removal of the wash buffer. The column will then be transferred into an RNase-free tube and 50  $\mu\text{L}$  of DNase/RNase-free water was added directly to the column matrix and centrifuged at top speed for 30 seconds to elute all RNA. The eluted RNA was put back in the same column and centrifuged at top speed for 30 seconds to increase the quantity of RNA recovered. The total RNA was measured and analyzed for purity using a full spectrum analysis at 400nm – 800nm using the Cary 50 spectrophotometer (Agilent, Corp.). The overall quality of an RNA preparation was assessed by electrophoresis on a 1.5% native agarose gel. The presence of a 28S and 18S ribosomal RNA bands indicated intact RNA. The  $A_{260}$  value was multiplied by the conversion factor of 40  $\mu\text{g}/\text{mL}$  and the value of 10 (to correct for the path length of 0.1 mm) to determine the concentration of RNA as described in the following formula:

$$\text{Concentration of RNA} = A_{260} \times 40 \mu\text{g}/\text{mL} \times 10 \times \text{Dilution factor}$$

### **cDNA synthesis for qRT-PCR**

The cDNA was synthesized using the Quantabio qScript™ cDNA synthesis kit (Quanta Bioscience, Inc Beverly, MA) from each experimental set using 800 ng of purified total RNA. A reaction mix was prepared containing qScript reaction (5X), qScript reverse transcriptase and nuclease-free water as shown in the Table 1.

Table 1. cDNA Mix

	Volume	Final concentration
5X qScript reaction mix	2 $\mu$ L	1X
qScript reverse transcriptase	0.5 $\mu$ L	1X
Nuclease-free Water	5 $\mu$ L	
Template RNA	2.5 $\mu$ L	800 ng
TOTAL VOLUME	10 $\mu$ L	

The samples were then placed into the BioRad MyCycler™ Thermal Cycler (Hercules, CA) for 5 minutes at 22°C, 30 minutes at 42°C followed by a cycle of 85°C for 5 minutes.

## Optimization of cDNA for qRT-PCR assays

Previous qRT-PCR experiments were used to analyze purified cDNA products; however, the recovery percentage was low and most experts in the field suggested not to clean up and purify the cDNA products. Upon receiving this advice, the efficiencies of three cDNA clean up kits (Zymo One Step PCR Inhibitor Removal, Zymo Research DNA Clean & Concentrator™ - 5, Monarch® PCR & DNA Cleanup Kit) were analyzed and compared to cDNA that had not been separated from the reverse transcription reaction mix.

### *Zymo One Step PCR Inhibitor Removal*

Zymo One Step PCR Inhibitor Removal Catalog # D6030 (Zymo Research Irvine, CA) was used to clean cDNA to remove any PCR inhibitors for more efficient qRT-PCR results. The Zymo-Spin™ III-HRC column was prepared prior to use by inserting into a collection tube, then adding 600 µL of Prep-Solution and centrifuging for three minutes at 8,000 x g. The column was then transferred to a nuclease free 1.5 mL microcentrifuge tube. At least 1 µg of DNA was needed in a volume ranging from 50 – 200 µL; therefore, to ensure a high yield of cDNA, 2 µg of cDNA (1:50 ratio of cDNA to nuclease free water), 10.5 µg of cDNA (1:10 ratio of cDNA to nuclease free water), and 11.4 µg of cDNA (1:5 ratio of cDNA to nuclease free water) in a total volume of 100 µL were used. The 100 µL of each respective cDNA concentration was added to separately prepared Zymo-Spin™ III-HRC columns and centrifuged for three minutes at 16,000 x g. The filtered

cDNA concentration was then quantified using the Cary 50 spectrophotometer. The  $A_{260}$  value was multiplied by the conversion factor of 33  $\mu\text{g}/\text{mL}$  and the value of 10 (to correct for the path length of 0.1 mm) to determine the concentration of RNA as described in the following formula:

$$\text{Concentration of cDNA} = A_{260} \times 33 \mu\text{g}/\text{mL} \times 10$$

*Zymo Research DNA Clean & Concentrator™ - 5*

The Zymo Research DNA Clean & Concentrator™ - 5 catalog # D4003S (Zymo Research Irvine, CA) was used to purify the cDNA. For DNA hydrolysis 3.6  $\mu\text{L}$  of 0.5 M EDTA and 3.6  $\mu\text{L}$  of 1N NaOH was added to 18  $\mu\text{L}$  of cDNA and incubated at 65°C for 15 minutes. Following incubation, 176.4  $\mu\text{L}$  (7 volumes) of DNA binding buffer was added to the reaction and mixed well. The mixture was then transferred to a Zymo-Spin column in a collection tube and centrifuged for 30 seconds at 16,000 x *g*. The flow through was discarded and 200  $\mu\text{L}$  of DNA wash buffer was added to the column then centrifuged for 30 seconds at 10,000 x *g*. This step was repeated and 10  $\mu\text{L}$  of DNA elution was then added directly to the column matrix and incubated at room temperature for 1 minute. The column was then transferred to a nuclease free 1.5 mL microcentrifuge tube and centrifuged for 30 seconds at 10,000 x *g*. The purified cDNA was quantified as described above.

### *Monarch® PCR & DNA Cleanup Kit*

The Monarch® PCR & DNA Cleanup Kit catalog # T1030L (New England Biolabs® Inc. Ipswich, MA) was used to purify the cDNA. The cDNA was diluted using 300 µL of DNA binding buffer then 300 µL of cold 100% Ethanol was added and mixed well by pipetting up and down. The column was placed into the collection tube and 450 µL (2 columns per treatment) of the sample mixture was loaded onto the column and centrifuged for one minute at 16,000 x *g*. The column was then removed and placed into a new collection tube where 500 µL of DNA wash buffer was added. It was then centrifuged for 1 minute at 16,000 x *g* and the flow through was discarded. The previous step was repeated but centrifuged for 2 minutes. The column was transferred to a nuclease free 1.5 mL microcentrifuge tube then 10 µL of elution buffer was added to the center of the matrix and incubated for 1 minute at room temperature. The column was centrifuged for 1 minute at 16,000 x *g*. The flow through was then added to the same matrix and centrifuged again for 1 minute at 16,000 x *g*. The purified cDNA was quantified as described above.

### *PCR*

The tubes were quickly tap-spun and 5 µL of the resulting products were run on a 1.5% agarose gel (0.75g Molecular Biology Certified agarose (IBI Scientific, Peosta, CA), 50 mL 1X TAE (Apex BioResearch Products, Genesee Scientific, San Diego, CA), 5 µL SYBR® Green I nucleic acid gel stain (Molecular

Probes, Eugene, OR) alongside the Apex 100 bp-Mid DNA marker (Genesee Scientific, San Diego, CA) for 1 hour at 100 volts using the BioRad PowerPac and Mini-Sub Cell GT (BioRad Laboratories, Hercules, CA). The gel was visualized on the Typhoon FLA 9000 (GE Healthcare Life Sciences, Uppsala, Sweden) using the following settings: Fluorescence, EtBr, 100  $\mu$ M.

### **Efficiency Assays**

A BioRad CFX96 Real-Time System C1000 Thermal Cycler Instrument (Hercules, CA) and the 2X Forget-Me-Not™ Universal Probe qPCR Master Mix (Biotium, Fremont, CA) that contained all necessary components were used to perform DNA-binding dye based real-time DNA amplification experiments. Primers were designed using IDT PrimerQuest Tool or IDT Predesigned qPCR Assays (Integrated DNA Technologies, Coralville, IA) and purchased from IDT. The respective forward and reverse primer pairs were used in the qRT-PCR (Table 2). The efficiency assays were performed in duplicate with cDNA dilutions that were plated in concentrations of 200 ng, 100 ng, 50 ng, 25 ng, 12.5 ng, and 6.25 ng/well with the appropriate 0.25  $\mu$ L forward and reverse primers, 5  $\mu$ L 2X Forget-Me-Not™ Universal Probe qPCR Master Mix and 2.5  $\mu$ L RNase and DNase free water. The primers used were purchased from Integrated DNA Technologies (Coralville, IA); Table 2 shows the primers used with the sequences, reference numbers, and base pairs sizes of the products.

Table 2. Primer sets for qRT-PCR

Genes	Primer name	Primer sequence 5'-3'	Size (bp)	Ref Number
<b>GAPDH*</b>	GAPDH For	GAGTCCACTGGCGTCTTCA	190	NM_001289746.1
	GAPDH Rev	GGGGTGCTAAGCAGTTGGT		
<b>FASN</b>	FASN For	TGTCCTGGGAGGAGTGATAA	119	NM_004104
	FASN Rev	CTGCTCCACGAACTCAAACA		
<b>HMGCR</b>	HMGCR For	TGAAGGGTTCGCAGTGATAAA	115	NM_000859
	HMGCR Rev	CCTGGACTGGAACGGATATAAA		
<b>PPARD</b>	PPARD For	CCGCAAACCCTTCAGTGATA	110	NM_006238.4
	PPARD Rev	GAATGATGGCCGCAATGAATAG		
<b>LDLR</b>	LDLR For	GGATCCTGTTCATGGCTTCA	102	NM_000527
	LDLR Rev	TCAGTCACCAGCGAGTAGAT		
<b>AGPAT4</b>	AGPAT4 For	CCCTTGGTTGCCAGAGATAAA	103	NM_020133.2
	AGPAT4 Rev	CACCACAGATGACCCAGAAA		
<b>Perilipin 4</b>	PLIN4 For	GAGTCACTGGTGCCGTAAT	100	NM_001080400.1
	PLIN4 Rev	CCAGTAGTCACTGCATCCTTAG		
<b>PRKAB2</b>	PRKAB2 For	GGATTTGGAGGACTCCGTAAG	100	NM_005399.3
	PRKAB2 Rev	GTTGAAGGACCCAGAGATGAAG		
<b>ETNK1</b>	ETNK1 For	CACTGAGCCATTGCTGATAGA	131	NM_18638.4
	ETNK1 Rev	CTGCATAGTCCCAGAGCTAAAG		
<b>MSMO1</b>	MSMO1 For	GGCAAGATGCTTTGGTTGTG	125	NM_006745.3
	MSMO1 Rev	CAAATGGAGCCTGAAACTCATG		
<b>B2M (1)</b>	B2M For	GGAAGTGGTCTTTCTATCTTTGT	143	NM_004048
	B2M Rev	ACCTCCATGATGCTGCCTAC		
<b>LRP12 (1)</b>	LRP12 For	CGTTGCTCTTGCTTTTCCTC	129	NM_013437
	LRP12 Rev	CACTTGGTGCTCGTATTTGC		
<b>IL4 (1)</b>	IL4 For	CAGTTCTACAGCCACCATGAG	94	NM_172348
	IL4 Rev	GTTTCAGGAATCGGATCAGC		
<b>COLEC12 (1)</b>	COLEC12 For	GCATGGTCAGCTCATCAAGA	123	NM_130386
	COLEC12 Rev	TCTCCTTTCTGTCCCTTGTTG		

Table 2. Primer Sets for qRT-PCR (continued)

<b>CETP (1)</b>	CETP For	GAAGGCCATGATGCTCCT	145	NM_000078
	CETP Rev	CTTGAAGACCACAGACACGTT		
<b>ANGPTL3 (1)</b>	ANGPTL3 For	ACGTGGGAGAACTACAAATATGG	98	NM_014495
	ANGPTL3 Rev	ACATAATTAGATTGCTTCACTATGGAG		
<b>B2M (2)</b>	B2M For	CCAGCATACTCCAAAGATTCA	94	NM_004048
	B2M Rev	TGGATGAAACCCAGACACATAG		
<b>LRP12 (2)</b>	LRP12 For	GGAGAGACTCCAGAGCAAATAC	104	NM_013437
	LRP12 Rev	GCCCTTATGAACCAGCTACA		
<b>IL4 (2)</b>	IL4 For	CCTCACATTGTCCTGCAAATC	122	NM_172348
	IL4 Rev	AGGTGATATCGCACTTGTGTC		
<b>COLEC12 (2)</b>	COLEC12 For	GGATACGCTGGAGAAGTTACAG	101	NM_130386
	COLEC12 Rev	CAGTGGTGATGAGGAAAGAGTTA		
<b>CETP (2)</b>	CETP For	ACTGCTACCTGTCTTTCCATAAG	104	NM_000078
	CETP Rev	CTTCAGGGTGAAGGAGATGAAA		
<b>ANGPTL3 (2)</b>	ANGPTL3 For	GCCAAGAGCACCAAGAACTA	117	NM_014495
	ANGPTL3 Rev	CCACTTGTATGTTACCTCTGT		

\* Efficiency assay was previously performed using this primer set with cDNA from HT29.f8 cells

The following thermal cycling conditions were used:

Table 3. Thermal cycling parameters for efficiency assays

Cycle Step	Temperature	Time	Cycles
Initial Denaturation	95°C	60 seconds	1
Denaturation	95°C	15 seconds	45
Extension	60°C	30 seconds (+plate read)	
Melt Curve	60 - 90°C	Increments of 0.5°C for 5 seconds (+plate read)	1

The Ct values obtained were exported into Microsoft Excel and the logarithm of the initial cDNA template concentration was plotted on the x axis and the Ct is plotted on the y axis per primer set (GOI). A standard curve was created and the equation and R<sup>2</sup> inserted. The slope from the generated equation was inserted into the following equation in order to determine the efficiencies.

$$E=10(-1/slope)^{-1} \times 100 \text{ to determine \% efficiency}$$

### **Real-time Quantitative Reverse Transcription PCR Assays (qRT-PCR)**

To determine if A3 treatment of RV-infected cells affected lipid metabolism, qRT-PCR assays were performed on genes noted as important in lipid metabolism using a BioRad CFX96 Real-Time System C1000 Thermal Cycler Instrument as described above for the efficiency assays. Briefly, at 8 hpi, total RNA was extracted from HT29.f8 cells using the Zymo Research Quick-RNA MiniPrep kit and complementary DNA (cDNA) was synthesized using the Quantabio qScript™ cDNA synthesis kit. The experiment was performed in triplicate with the use of 2X Forget-Me-Not™ Universal Probe qPCR Master Mix. Each reaction mixture contained 5 μL 2X Forget-Me-Not™ Universal Probe qPCR Master Mix, 0.25 μL of 10 μM forward and reverse primers, 50 ng of template DNA and nuclease-free water to a final volume of 10 μL. The housekeeping genes used for relative gene expression analyses were GAPDH and B2M. The qRT-PCR analysis was performed using the BioRad CFX96 Real-Time System

C1000 Thermal Cycler Instrument. The qRT-PCR cycle conditions that were used are described in Table 4.

Table 4. PCR cycle conditions

Cycle Step	Temperature	Time	Cycles
Initial Denaturation	95°C	60 seconds	1
Denaturation	95°C	15 seconds	45
Extension	60°C	30 seconds (+plate read)	
Melt Curve	60 - 90°C	Increments of 0.5°C for 5 seconds (+plate read)	1

The obtained threshold values (Ct) from the qRT-PCR experiment were exported to excel for data analyses. The fold change in signal of expression of the genes analyzed was determined using the Livak method ( $2^{-\Delta\Delta C_t}$ ) relative to GAPDH and B2M (Livak and Schmittgen, 2001). The results for each treatment were averaged and were statistically evaluated by analysis of variance (ANOVA) and Student's t two tailed tests using Microsoft Excel 2016 software (significance level,  $p \leq 0.05$ ). The results were expressed as the mean  $\pm$  standard deviation (SD).

## **Whole Cell Histochemical and Immunofluorescent Assays**

### *Histochemical Staining*

The neutral fats and nuclei of HT29.f8 cells were histochemically stained to analyze the distribution and accumulation of neutral fats within the cells. Briefly, cells were grown to 80% confluence in 8-well slides (Lab-Tek Chamber Slide System, Nunc, Inc. Naperville, IL) and RV-infected and treated with arachidin-3 as described above, RV alone, RV with 20  $\mu$ M A3, 20  $\mu$ M A3 alone, and cells without treatments (NV-no virus). At 18 hpi, the cells were washed with PBS 1X one time at 25°C, and then fixed with 1% Glutaraldehyde (Electron Microscopy Science, Hatfield, PA) for one hour at 25°C in a fume hood. Following fixation, the cells were washed twice with PBS 1X at 25°C and 300  $\mu$ Ls of filtered 0.12% Oil Red O stain was added to each well. The chambered slides were then rotated to ensure even coverage of the stain on the cells. The Oil Red O incubated for 5 minutes then was removed and rinsed with  $ddH_2O$  until the solution removed became clear (~ 5 washes). Following the removal of the last  $ddH_2O$  wash, 300  $\mu$ Ls of 0.12% of hematoxylin stain was added to each well and slowly rotated to ensure even coverage of the stain on the cells. The hematoxylin stain incubated for 1 minute then was removed and rinsed with warm  $ddH_2O$  until the solution removed became clear (~5 washes). The last wash of  $ddH_2O$  was removed and the slide was mounted in 1X PBS. The cells were then viewed using the Olympus BX50 with DP Manager System compound light microscope with the DP71 camera (Olympus Corporation, Shinjuku, Tokyo, Japan) equipped

with a X10 objective. The images were digitized using the DP Controller software (Olympus Corporation).

### *Immunofluorescent Assays*

The nucleus, plasma membrane, and lipid droplets of HT29.f8 cells were fluorescently labelled to analyze the distribution and accumulation of neutral fats within lipids droplets. Briefly, cells were grown to 80% confluence in 8-well slides and RV-infected and treated with A3 as described above (NV, RV, RV+A3, and A3). At 8 hpi, the cells were washed with PBS 1X one time at 25°C, and then fixed with 1% Glutaraldehyde for one hour at 25°C in a fume hood. Following fixation, the cells were washed twice with PBS 1X at 25°C. The LipidSpot™ (Biotium) was used to label the lipid droplets by adding 200 µLs of 1:500 dilution of 1000X stock solution in DMSO made with 1X PBS to each well and incubated for 10 minutes in the dark. The wells were then washed twice with 1X PBS. The Image-IT™ LIVE Plasma Membrane and Nuclear Labeling Kit (I34406) (Molecular Probes, Invitrogen detection Technologies, Eugene, OR) was then used to label the cells. Briefly, one solution for the single step staining for both stains was prepared by adding 5.0 µg/mL Alexa Flour® 594-labeled wheat germ agglutinin and 1 µM Hoechst 33342 stain into 1X PBS. Two hundred µLs of the labelling solution was added to each well in 8-well chambered slides, incubated for ten minutes at 25°C, removed and the cells were washed twice with PBS 1X, and mounted in PBS 1X. The microscopic analysis was carried out using the Olympus BX50 with DP Manager System compound light microscope with

epifluorescent illumination for Alexa Flour® 594-labeled wheat germ agglutinin (Excitation 25 480-550 nm, dichroic mirror DM 570 nm, barrier filter 590 nm), Hoechst 33342 (Excitation 330-385 nm, dichroic mirror DM 400 nm, barrier filter BA420nm), and LipidSpot™ 488 (Excitation 420-480 nm, dichromic mirror DM 500 nm, barrier filter 515 nm) with the DP71 camera equipped with X40 and X100 objectives.

The nuclei and NSP4 in RV-infected HT29.f8 cells were fluorescently labelled to confirm infection. Briefly, cells were grown to 80% confluence in 8-well slides and RV-infected and treated with A3 as described above (NV, RV, RV+A3, and A3). At 8 hpi and 18 hpi the cells were washed with cold 1X PBS then cold acetone/methanol (1:1) was added and incubated until the solution came to room temperature (~ 5 minutes). The acetone/methanol (1:1) was removed and wells were washed once with 1X PBS. Following the removal of the 1X PBS, 200 µL of filtered blocking buffer (1X PBS + 0.25% BSA) was added to each well and incubated overnight with rocking at 4°C. After incubation the blocking buffer was removed and 200 µL of polyclonal rabbit sera anti-NSP4<sub>150-175</sub> diluted in blocking buffer at 1:250 dilution was added to each well and incubated at room temperature with rocking for one hour. The primary antibodies were then removed, and cells were washed four times with 1X PBS. Then the secondary antibody, 8µg/mL Goat Anti-Rabbit IgG H&L (Alexa Fluor 488) catalog # ab150081(Abcam, Cambridge, UK) was added and incubated at room temperature for 30 minutes. The cells were then washed four times with 1X PBS.

The Image-IT™ LIVE Plasma Membrane and Nuclear Labeling Kit was then used to label the nucleus. Briefly the nuclear stain was prepared with 1  $\mu$ M Hoechst 33342 stain in 1X PBS. After removing the last wash of 1X PBS, 200  $\mu$ Ls of the Hoechst 33342 stain was added to each well in 8-well chambered slides, incubated for ten minutes at 25°C, removed and the cells were washed twice with PBS 1X, and mounted in PBS 1X. The microscopic analysis was carried out using the Olympus BX50 with DP Manager System compound light microscope with epifluorescence illumination for Hoechst 33342 (Excitation 330-385nm, dichroic mirror DM 400 nm, barrier filter BA420 nm) and Goat Anti-Rabbit IgG H&L (Alexa Fluor 488) (Excitation 420-480 nm, dichromic mirror DM 500 nm, barrier filter 515 nm) with the DP71 camera equipped with X40 and X100 objectives.

### **Western Blot Analyses**

To determine the expression and regulation of critical proteins in lipid metabolism, HT29.f8 cell lysates with treatments and controls (NV, RV, RV+A3, and A3) were probed with protein specific primary and fluorescently labeled secondary antibodies. The primary antibodies were to bind the specific proteins followed by the addition of goat anti-rabbit IgG Alexa Fluor® 546-labeled antibody (Life Technologies, Carlsbad, CA) to detect the cellular and viral proteins encoded by regulated genes of interest. The concentrations of protein and antibodies used is shown in Table 5.

Table 5. Antibodies used in western blot analysis

Concentration of Cell lysates	Primary Antibody (1°) (concentration)	Catolog #	1° concentration: 2° concentration (2 mg/mL)
30 µg	Rabbit anti-Perilipin 1 (1.1 mg/mL)	Novus Biologicals (Centennial, CO) NB110-40760	1:550 : 1:500
40 µg	Rabbit anti – TIP47 (sera)	Novus Biologicals NB110-40765	1:2500 : 1:5000
40 µg	Rabbit anti- ACAT	GeneTex (Irvine, CA) GTX102637	1:1000 : 1:5000 1:1000 : 1:2500 1:1000 : 1:1000 1:750 : 1:1000 1:750 : 1:500 1:500 : 1:500 1:250 : 1:500
40 µg	Rabbit anti-DGAT1 (0.5 mg/mL)	BioVision (Milpitas, CA) 3845-30T	1:1000 : 1:1000 1:750 : 1:1000 1:500 : 1:1000 1:500 : 1:500 1:250 : 1:500
20 µg	Mouse (Mab) anti-DGAT	Santa Cruz Biotechnologies (Dallas, TX) sc-271934	1:200 : 1:5000 1:500 : 1:5000
20 µg	Mouse (Mab) anti-adrp	Santa Cruz Biotechnologies (Dallas, TX) sc-377429	1:500 : 1:5000

The HT29.f8 cell lysate proteins was separated by 12% Mini-PROTEAN® TGX Stain-Free™ gels (Bio Rad) in 25 mM Tris/192 mM glycine/0.1% SDS buffer (Bio Rad) at 150 V for approximately 50 minutes in the Mini-PROTEAN® Tetra System (Bio Rad). After electrophoresis, proteins were transferred to a nitrocellulose membrane. Briefly, a transfer sandwich was constructed of 1 filter

pad, a blot absorbent filter paper (Thermo Scientific), a 0.45  $\mu\text{m}$  nitrocellulose membrane (GE Amersham™ Protran™), the SDS-PAGE, blot absorbent filter paper, and a filter pad within a cassette. The cassette was placed in a Mini-PROTEAN® Tetra System (Bio Rad) with a stir bar at the bottom containing and completely being covered with electroblotting buffer (25 mM Tris/192 mM glycine/20% (w/v) methanol). The system was placed in a large container and covered in ice to prevent overheating on a magnetic stirrer while running for 1 hour at 500 mA. Upon removal of the nitrocellulose membrane, nonspecific binding of antibodies was blocked with incubation in 5% nonfat dry milk in TBS + 0.05% Tween 20 overnight at 4°C with rocking. The nitrocellulose membrane was incubated with protein specific primary antibodies overnight at 4°C with rocking. The nitrocellulose membrane was washed with TBS + 0.05% Tween 20 (four times) for 10 minutes each while rocking. The fluorescently labeled secondary antibody was then added to the membrane to incubate for 45 minutes at room temperature with rocking. Following another series of washes as described above, the membranes were visualized using the 556 nm excitation laser and 573 nm emission filter on the typhoon 9500 plus laser scanner (GE Life Sciences Marlborough, MA).

## RT<sup>2</sup> Profiler PCR Array

The human lipoprotein and cholesterol metabolism RT<sup>2</sup> Profiler PCR Array was used to analyze the expression of 84 key genes involved in signaling pathways. HT29.f8 cells infected with no virus, RV only, RV with A3, and A3 only were used for total RNA extraction using Zymo Research Quick-RNA MiniPrep kit (Zymo Research Irving, CA) and quantification using the Cary 50 spectrophotometer. The total RNA was reverse transcribed using RT<sup>2</sup> First Strand kit (Qiagen, Valencia, CA). The resulting cDNA mixture (20  $\mu$ L per sample) was diluted in 91  $\mu$ L of nuclease-free water (Qiagen). The diluted cDNA (102  $\mu$ L) was mixed with the PCR components mix composed of 1,248  $\mu$ L of water plus 1,350 of 2X RT<sup>2</sup> SYBR green RT<sup>2</sup> master mix. The mixture was dispensed at 25  $\mu$ L per well into a 96-well RT<sup>2</sup> Profiler PCR array plate. DNA amplification was carried out with a BioRad CFX96 Real-Time System C1000 Thermal Cycler Instrument (Hercules, CA) using the cycling conditions shown in Table 6.

Table 6. PCR cycling conditions for RT<sup>2</sup> Profiler PCR Array

Cycle Step	Temperature	Duration	Cycles
Activation	95°C	10 minutes	1
Fluorescence data collection	95°C	15 seconds	40
	60°C	1 minute	

The specificity of the primer sets was determined by melting curve analyses of the amplicons. The resulting  $C_T$  values for the plate were exported to an Excel worksheet. The fold changes of gene expression were calculated based on the  $\Delta\Delta C_T$  method with normalization of the raw data to GAPDH and B2M.

## RESULTS

### Optimization of cDNA for qRT-PCR assays

Before the qRT-PCR assays were performed, the annealing temperatures were optimized for the primer sets (HGMCR, FASN, LDLR, and PPARD) using a gradient PCR experiment at the following temperatures: 62°C, 59.1°C, 55.5°C, and 52.9°C. cDNA was purified using the Monarch® PCR & DNA Cleanup Kit from New England BioLabs® Inc. as previously described in the Parr laboratory (Napier-Jameson, 2018). The HMGCR and LDLR PCR products were visualized on a 1.5% agarose gel; however, for FASN and PPARD no banding pattern was observed (Figure 7). After determining the recovery rate of the cDNA from the Monarch® PCR & DNA Cleanup Kit was only 7.9%, concerns were raised that genes transcribed at low levels would not be represented using this purified cDNA. Therefore, three different methods of purifying cDNA were used and compared to unprocessed cDNA following reverse transcription to optimize the quantity and quality of cDNA for further use in qRT-PCR assays. The Monarch® PCR & DNA Cleanup Kit from New England BioLabs® Inc. showed a 7.9% cDNA recovery; the Zymo One Step PCR Inhibitor Removal Kit from Zymo Research showed a 7.2% recovery, and the Zymo Research DNA Clean & Concentrator™ - 5 Kit showed a 0% recovery (appendix Table 10). Next the recovered cDNA from the Monarch® PCR & DNA Cleanup Kit, Zymo One Step PCR Inhibitor Removal

Kit, and unprocessed cDNA were used with GAPDH primer set to perform PCR experiments and the amplicons were visualized on a 1.5% agarose gel. Using the Monarch® PCR & DNA Cleanup Kit a non-specific banding pattern alongside the gene specific band (98 bp) was observed; however, only one gene specific band was observed using both Zymo One Step PCR Inhibitor Removal Kit and unprocessed cDNA (Figure 8). Although the banding pattern of the Zymo One Step PCR Inhibitor Removal Kit and unprocessed cDNA were similar, the recovery rate for the Zymo kit was only 7.2% (appendix Table 10). Then the unprocessed cDNA for both NV and RV treatments were used with the primer sets (HMGCR, FASN, LDLR, and PPARD) to perform PCR at 58°C. The amplicons were visualized for HMGCR, FASN, LDLR, and PPARD at bp sizes 115, 119, 102, 110, respectively (Figure 9) and compared to the gradient PCR experiment (Figure 7).

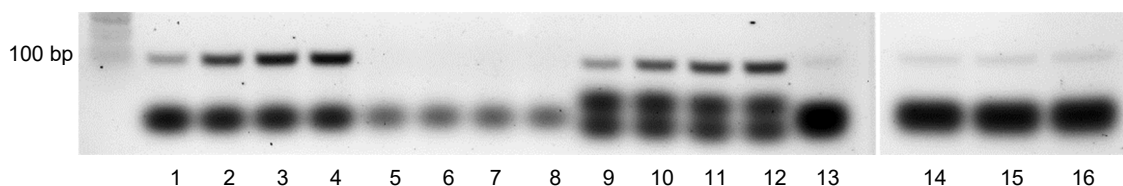


Figure 7. Gradient PCR assay products at 62°C, 59.1°C, 55.5°C, and 52.9°C with cDNA from Monarch® PCR & DNA Cleanup Kit from New England BioLabs® Inc. Lanes 1 – 4 HMGCR PCR products at ~115 bp. Lanes 5 – 8 FASN PCR products not visible. Lanes 9 – 12 LDLR PCR products at ~102 bp. Lanes 13 – 16 PPARD PCR products at ~110 bp.

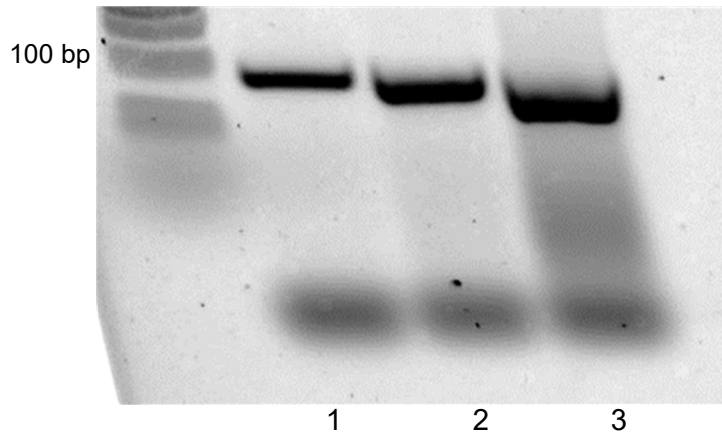


Figure 8. GAPDH PCR products (98 bp) using 1) unprocessed cDNA; 2) cDNA purified using Zymo One Step PCR Inhibitor Removal Kit; and 3) cDNA purified using Monarch® PCR & DNA Cleanup Kit. A 98 bp product was present in all 3 lanes. Lane 3 has non-specific banding patterns below 98 bp.

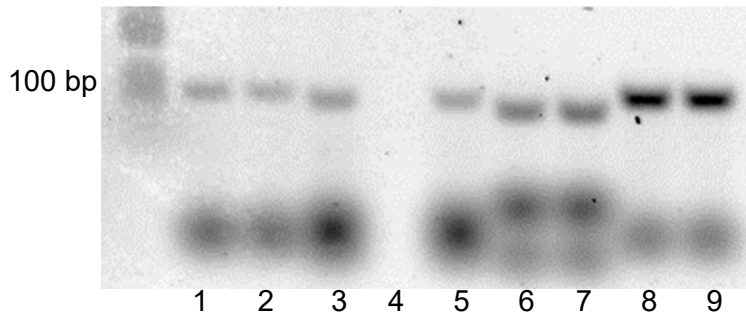


Figure 9. LDLR, HMGCR, PPARD, and FASN PCR assay products using unprocessed cDNA from NV and RV treatments. All reactions were performed at a 58°C annealing temperature. Lanes 1 (NV) and 2 (RV) LDLR PCR products at ~102 bp. Lanes 3 (NV) and 5 (RV) HMGCR PCR products at ~115 bp. Lanes 6 (NV) and 7 (RV) PPARD PCR products at ~110 bp. Lanes 8 (NV) and 9 (RV) FASN PCR products at ~119 bp.

## Efficiency Assays

The first efficiency assays were performed with the primer sets of specific genes found in the literature to be involved in the rate-limiting steps of lipid metabolism pathways (Davidson, 2018; Goldstein and Brown, 2009; Hussain, 2009; Radhakrishnan et al., 2007). The efficiencies of each gene are as follows: FASN 107.73%, HMGCR 95.68%, LDLR 97.52%, Perilipin 4 97.52%, PRKAB2 98.71%, ETNK1 93.10%, and MSMO1 110.64% (Table 7). The efficiencies of PPARD and AGPAT4 could not be calculated and therefore were dropped from the study.

After the RT<sup>2</sup> Profiler PCR Array data was analyzed (see below), pre-designed primers were obtained from IDT to confirm the changes of select genes [Table 2: B2M (1), LRP12 (1), IL4 (1), COLEC12 (1), CETP (1), ANGPTL3 (1)]. However, gradient PCR assays on each primer set were negative for PCR products. Even the positive control for B2M and ANGPTL3 were negative (data not shown) and with technical support from multiple IDT representatives, it was determined the primer sets were not functioning properly. Therefore, the efficiencies were unobtainable for these primer sets.

Following the negative results of the pre-designed primers from the second set, new primers were designed in house for each gene [Table 2: B2M (2), LRP12 (2), IL4 (2), COLEC12 (2), CETP (2), ANGPTL3 (2)]. Nonetheless, gradient PCR assays on each primer set were negative for PCR products except

B2M (2) (data not shown); therefore, the efficiencies were unobtainable for the remaining primer sets. The efficiency for B2M (2) was calculated to be 93.16% (Table 7).

Table 7. Primer efficiencies calculated for lipid metabolism genes and a housekeeping gene (B2M).

<b>Primer</b>	<b>Efficiencies</b>
GAPDH*	92.55
FASN	107.43
HMGCR	95.68
PPARD	
LDLR	97.52
AGPAT4	
Perilipin 4	101.35
PRKAB2	98.71
ETNK1	93.10
MSMO1	110.64
B2M (1)	
LRP12 (1)	
IL4 (1)	
COLEC12 (1)	
CETP (1)	
ANGPTL3 (1)	
B2M (2)	93.16
LRP12 (2)	
IL4 (2)	
COLEC12 (2)	
CETP (2)	
ANGPTL3 (2)	

\* Efficiency assay was previously performed using this primer set with cDNA from HT29.f8 cells

## Quantitative Real-time PCR Assays

To determine the effects on lipid metabolism in HT29.f8 cells treated with 1) RV; 2) RV+A3; and 3) A3, qRT-PCR experiments were performed on each treatment using total RNA collected 8 hpi (Figures 10 – 13).

ETNK1 showed little to no regulation across all treatments (RV  $0.936 \pm 0.03$ , RV+A3  $0.718 \pm 0.09$ , and A3  $0.869 \pm 0.06$ ) (Figure 10). There were no statistical differences between all treatments except RV+A3 was statistically different from A3 ( $P = 0.0397$ ).

HMGCR demonstrated an up-regulation with all treatments (RV  $2.055 \pm 0.16$ , RV+A3  $1.647 \pm 0.14$ , and A3  $1.172 \pm 0.081$ ) (Figure 11). RV was statistically different from RV+A3 ( $P = 0.029$ ) and A3 ( $P = .003$ ); and RV+A3 was statistically different from A3 ( $P = 0.014$ ).

Perilipin 4 demonstrated a down-regulation with all treatments (RV  $0.530 \pm 0.019$ , RV+A3  $0.368 \pm 0.094$ , and A3  $0.671 \pm 0.054$ ) (Figure 12). A3 was statistically different from RV ( $P = 0.034$ ) and RV+A3 ( $P = 0.015$ ).

LDLR demonstrated an up-regulation with RV ( $2.587 \pm 0.14$ ) and RV+A3 ( $2.047 \pm 0.10$ ); however, A3 ( $1.294 \pm 0.022$ ) showed little to no regulation (Figure 13). RV was statistically different from RV+A3 ( $P = 0.008$ ) and A3 ( $P = 0.003$ ); and RV+A3 was statistically different from A3 ( $P = 0.009$ ).

FASN, PRKAB2, and MSMO1 demonstrated Ct values above 35 for all treatments; therefore, the transcripts could not be detected using 50 ng of cDNA.

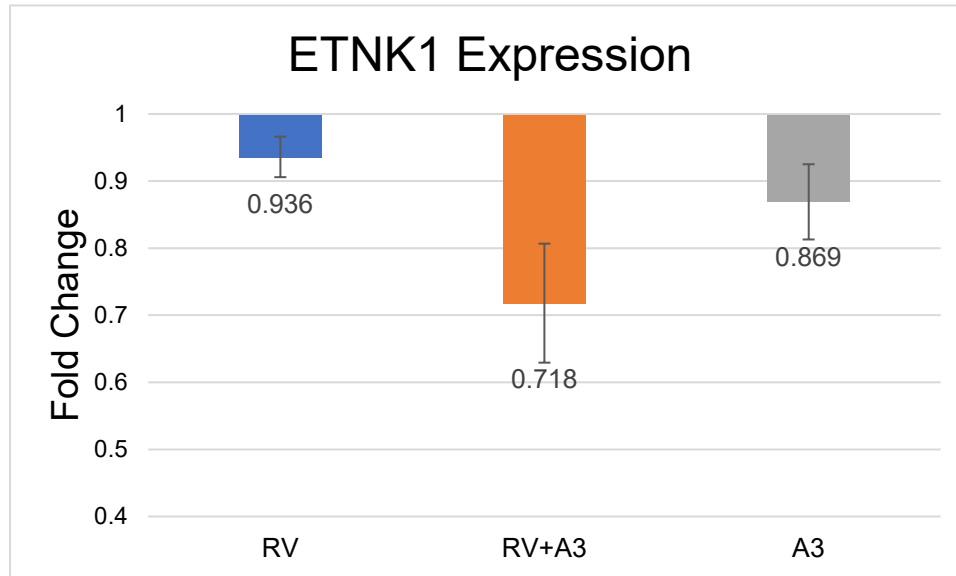


Figure 10. ETNK1 Expression in HT29.f8 cells at 8 hpi. HT29.f8 cells were infected with RV – Wa (MOI = 2) or mock-infected and treated with A3 for 1 h at 37°C. Total RNA was isolated from the cells treated with RV, RV + 20 µM A3, or 20 µM A3, and ETNK1 mRNA levels were measured by quantitative real-time RT-PCR assay. The levels of glyceraldehyde-3-phosphate dehydrogenase (GAPDH) and beta-3-microglobulin (B2M) were used to normalize the quantities of target mRNA. Fold changes in signals of expression of the gene of interest relative to GAPDH and B2M were calculated using the Livak method ( $2^{-\Delta\Delta Ct}$ ). Each column represents the mean  $\pm$  standard deviation (SD) from three separate experiments

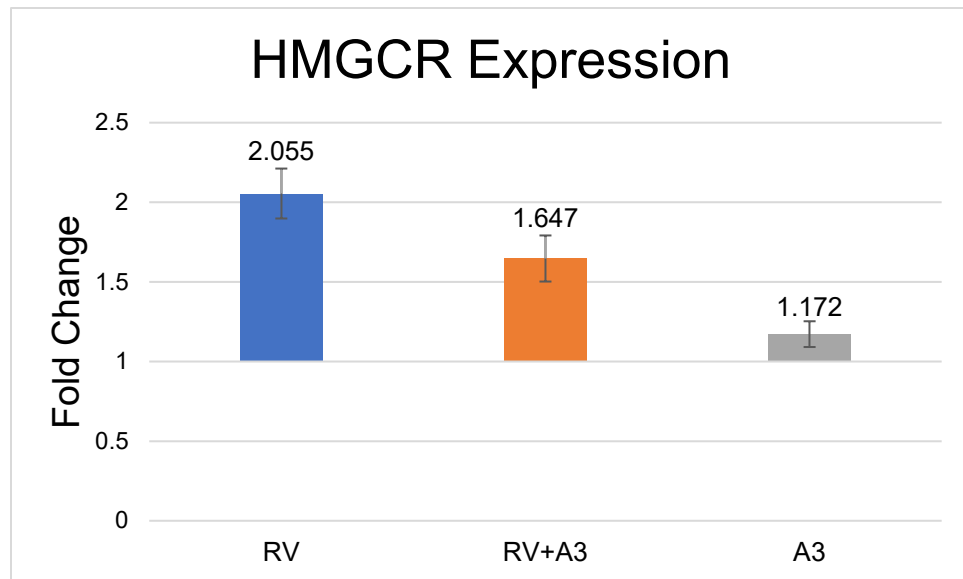


Figure 11. HMGCRC Expression in HT29.f8 cells at 8 hpi. HT29.f8 cells were infected with RV – Wa (MOI = 2) or mock-infected and treated with A3 for 1 h at 37°C. Total RNA was isolated from the cells treated with RV, RV + 20 µM A3, or 20 µM A3, and HMGCRC mRNA levels were measured by quantitative real-time RT-PCR assay. The levels of glyceraldehyde-3-phosphate dehydrogenase (GAPDH) and beta-3-microglobulin (B2M) were used to normalize the quantities of target mRNA. Fold changes in signals of expression of the gene of interest relative to GAPDH and B2M were calculated using the Livak method ( $2^{-\Delta\Delta C_t}$ ). Each column represents the mean  $\pm$  standard deviation (SD) from three separate experiments

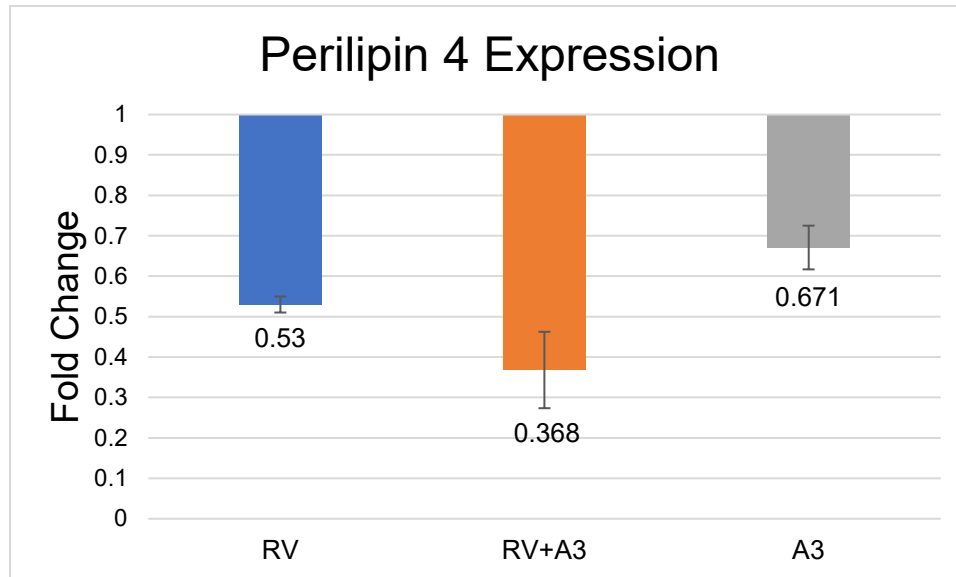


Figure 12. Perilipin 4 Expression in HT29.f8 cells at 8 hpi. HT29.f8 cells were infected with RV – Wa (MOI = 2) or mock-infected and treated with A3 for 1 h at 37°C. Total RNA was isolated from the cells treated with RV, RV + 20  $\mu$ M A3, or 20  $\mu$ M A3, and Perilipin 4 mRNA levels were measured by quantitative real-time RT-PCR assay. The levels of glyceraldehyde-3-phosphate dehydrogenase (GAPDH) and beta-3-microglobulin (B2M) were used to normalize the quantities of target mRNA. Fold changes in signals of expression of the gene of interest relative to GAPDH and B2M were calculated using the Livak method ( $2^{-\Delta\Delta C_t}$ ). Each column represents the mean  $\pm$  standard deviation (SD) from three separate experiments

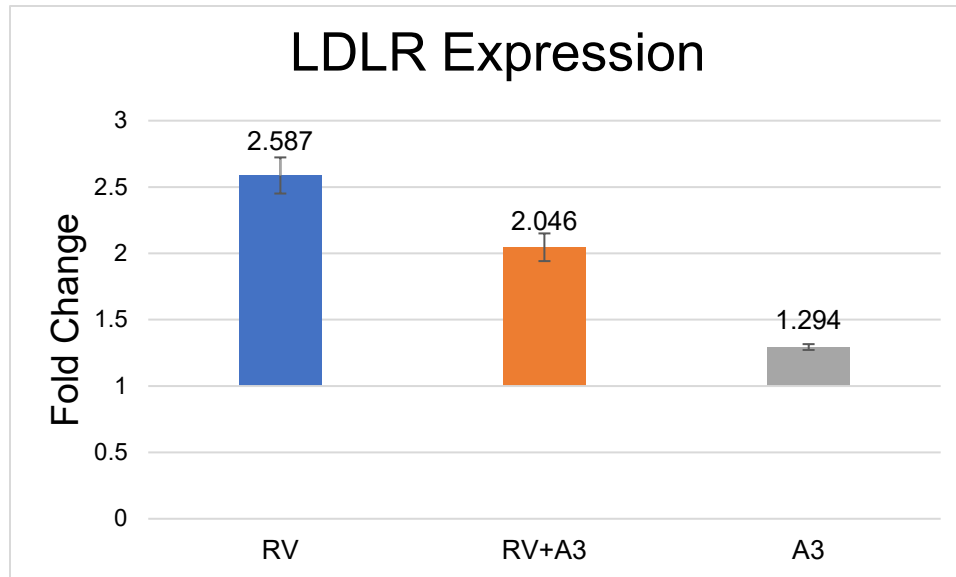


Figure 13. LDLR Expression in HT29.f8 cells at 8 hpi. HT29.f8 cells were infected with RV – Wa (MOI = 2) or mock-infected and treated with A3 for 1 h at 37°C. Total RNA was isolated from the cells treated with RV, RV + 20  $\mu$ M A3, or 20  $\mu$ M A3, and LDLR mRNA levels were measured by quantitative real-time RT-PCR assay. The levels of glyceraldehyde-3-phosphate dehydrogenase (GAPDH) and beta-3-microglobulin (B2M) were used to normalize the quantities of target mRNA. Fold changes in signals of expression of the gene of interest relative to GAPDH and B2M were calculated using the Livak method ( $2^{-\Delta\Delta C_t}$ ). Each column represents the mean  $\pm$  standard deviation (SD) from three separate experiments.

## **Histochemical staining**

To determine the distribution and accumulation of neutral fats in HT29.f8 cells treated with 1) NV; 2) RV; 3) RV+A3; and 4) A3, histochemical staining was performed with each treatment fixed at 18 hpi. Following cell fixation with 1% glutaraldehyde, Oil Red O was used to stain the neutral fats (red) while hematoxylin was used to counterstain the nucleus (blue).

Cells treated with NV exhibited a prominent staining of the nuclei (blue) and very little neutral fats (red) (Figure 14A). In comparison, A3 treated cells display prominent nuclei with an increase in neutral fat accumulation that appeared evenly distributed throughout the cells (Figure 14B).

In comparison to NV and A3 treated cells, those treated with RV, presented an elevated accumulation of neutral fats (red) as well as defined nuclei (Figure 14C). Interestingly, cells treated with RV+A3 displayed an increase in neutral fat accumulation compared to A3 treated cells (Figure 14D).

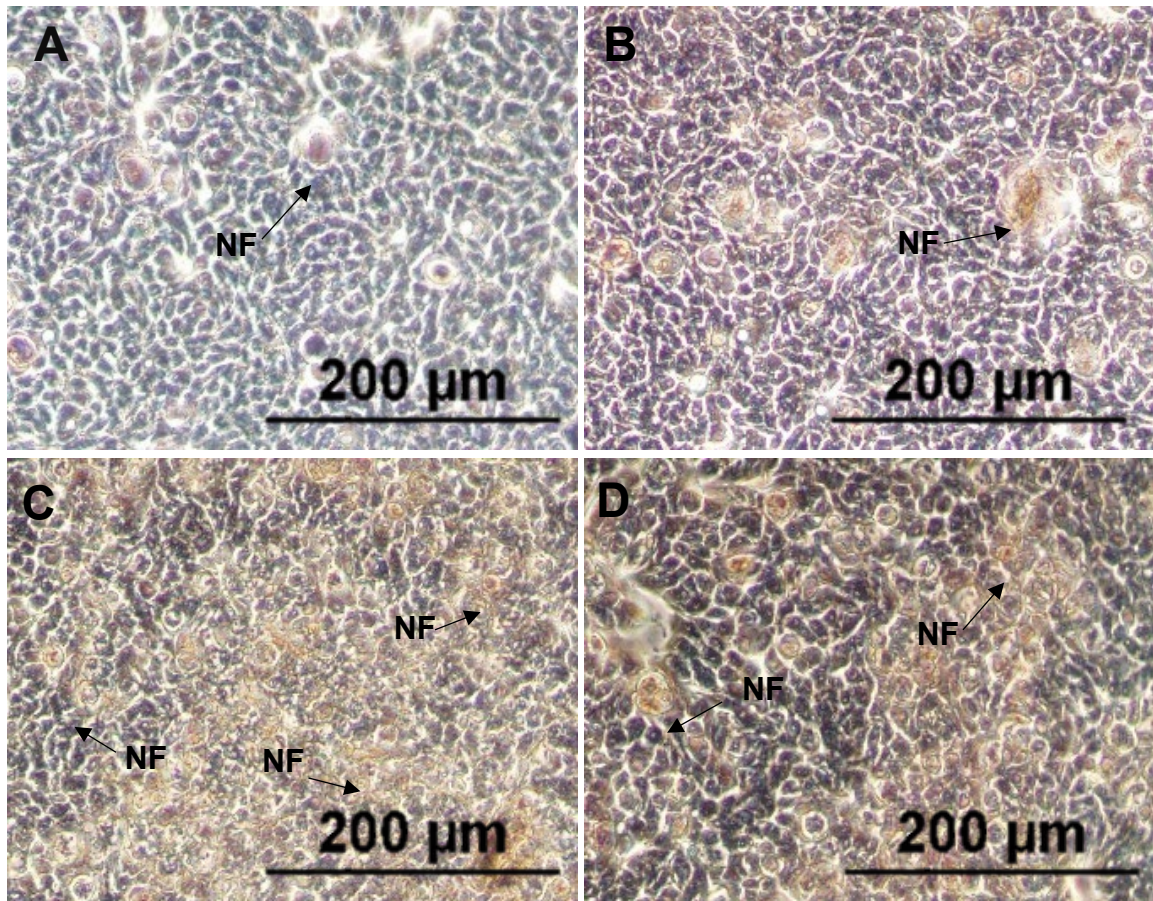


Figure 14. Differential histochemical staining of fixed HT29.f8 cells 18 hpi using Oil Red O (red) and Hematoxylin (blue). HT29.f8 cells were infected with RV at a MOI = 2 and treated with A3. At 18 hpi, the cells were fixed with 1% glutaraldehyde then stained using 0.12% oil red o stain and hematoxylin. The cells were then viewed and analyzed using the Olympus BX50 with DP Manager System compound light microscope with the DP71 camera. A: NV treatment demonstrated very little neutral fats (NF) and very prominent nuclei; B: Cells with 20µM A3 showed a slight increase in neutral fat accumulation; C: RV alone exhibited a dramatic increase in neutral fat accumulation giving the cells a more red appearance; D: Cells treated with RV and 20µM A3 show a similar appearance to RV alone. (X100)

## **Immunofluorescent Assays**

### *Lipid Droplet Staining*

To determine the distribution and accumulation of neutral fats that rapidly accumulate in lipid droplets, HT29.f8 cells treated with 1) NV; 2) RV; 3) RV+A3; and 4) A3, were immunofluorescently stained with LipidSpot™ 488. At 8 hpi, cells were fixed with 1% glutaraldehyde, stained as follows: LipidSpot™ 488 to visualize lipid droplets, Alexa Flour-594 labeled wheat germ agglutinin (WGA) to visualize plasma membranes, Hoechst 33342 dye to visualize the nucleus.

In cells treated with NV, demonstrated very distinct plasma membranes with neutral fats evenly distributed within the cell (Figure 15A). However, cells treated with A3 exhibited a disruptive pattern of the plasma membrane with an increase in neutral fats within the cytoplasm (Figure 15B). At the same time point, cells RV treated showed less distinct plasma membranes with an increase in neutral fats in comparison to NV and A3 (Figure 15C). The neutral fats appeared perinuclear and more distinct with RV treatment.

Additionally, cells treated with RV+A3 had distinct plasma membranes similar to the observations with NV and displayed an increased accumulation of neutral fats in comparison to A3 alone (Figure 15D). When compared to RV alone, RV+A3 had a more evenly distributed pattern of neutral fats.

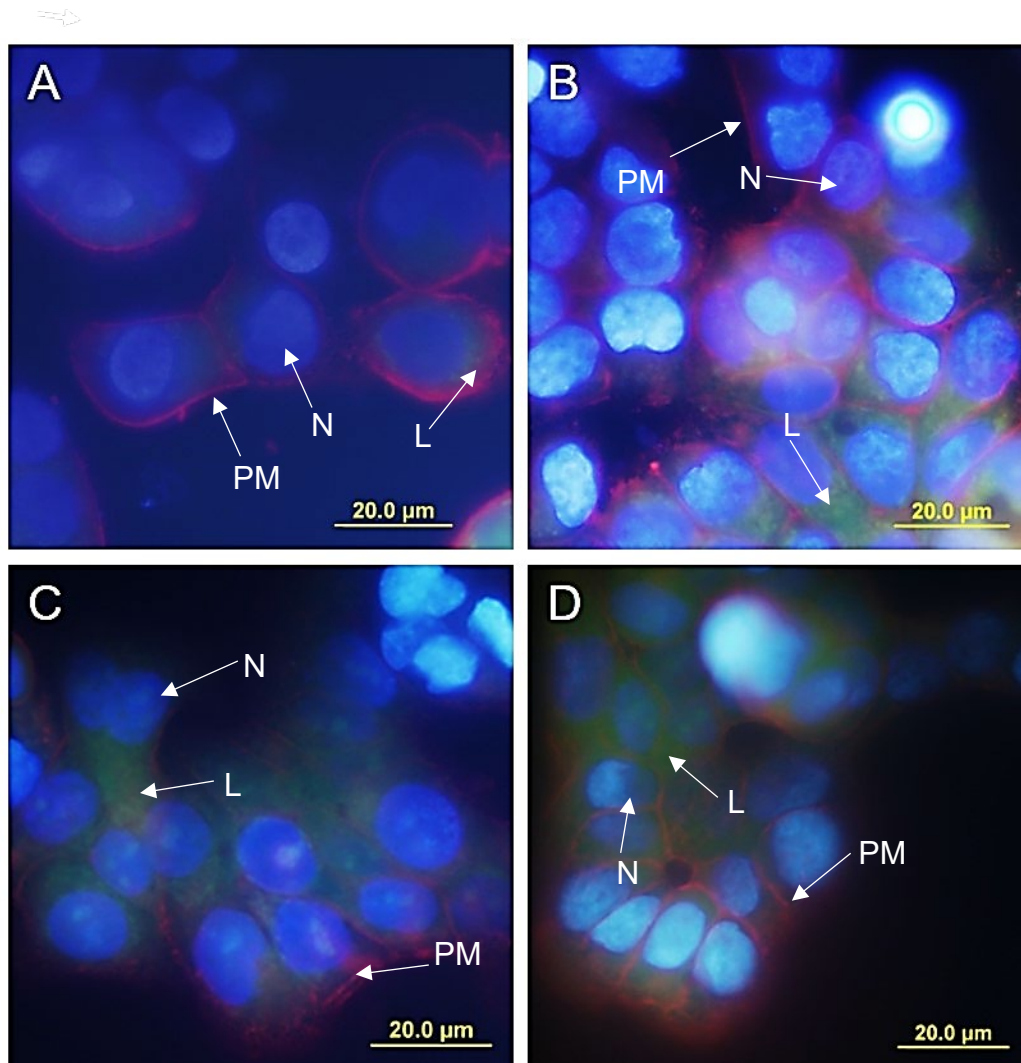


Figure 15. Qualitative comparison of lipid droplets in RV infected and A3 treated HT29.f8 cells. HT29.f8 cells were infected with RV at a MOI = 2 and treated with 20 $\mu$ M A3. At 8 hpi, the cells were fixed with 1% glutaraldehyde then labeled with Alexa Fluor<sup>®</sup> 594-labeled wheat germ agglutinin (WGA) which binds to the N-acetylglucosamine and N-acetylneuraminic (sialic) acid residues in membranes (red), Hoechst 33342 dye which is selective for DNA (blue), and a LipidSpot<sup>™</sup> 488 stain which is selective for the neutral lipids that rapidly accumulate in lipid droplets (green). A: NV cells showed prominent nuclei (N) and distinct plasma membranes (PM) with a small amount of lipid (L) in the cytoplasm; B: A3 treated cells displayed prominent nuclei with disrupted PM and large amounts of lipids in the cytoplasm; C: RV treated cells exhibited prominent nuclei, disrupted PM, and large amounts of lipids in the cytoplasm; D: RV+A3 treated cells demonstrated prominent nuclei and PM with an increase in lipids in the cytoplasm. (X400)

### *NSP4 Immunofluorescent Assays*

To confirm the expression of NSP4 in RV infected cells at 8 and 18 hpi, HT29.f8 cells were treated with 1) NV; 2) RV; 3) RV+A3; and 4) A3, then the nuclei and NSP4 were fluorescently labeled. Following cell fixation with 1% glutaraldehyde, the nuclei were labeled with Hoechst 33342 dye (blue) and sequentially probed with polyclonal rabbit sera anti-NSP4<sub>150-175</sub> and Goat Anti-Rabbit IgG H&L (Alexa Fluor 488) to show the presence of NSP4 (green).

At 8 hpi, the control treatments of NV or A3 alone (Figure 16A and 16B, respectively) showed no fluorescently labeled NSP4 and very distinct nuclei. In comparison, cells treated with RV or RV+A3 (Figure 16C and 16D, respectively) showed NSP4 located within the cytoplasm; however, there was a slight decrease in NSP4 fluorescence with RV+A3 treatment.

At 18 hpi, the control treatments of NV or A3 alone (Figure 17A and 17B, respectively) showed no NSP4 fluorescently labeled and very distinct nuclei. In comparison, cells treated with RV or RV+A3 (Figure 17C and 17D, respectively) showed NSP4 located within the cytoplasm; however, there was a slight decrease in fluorescence with RV+A3 treatment.

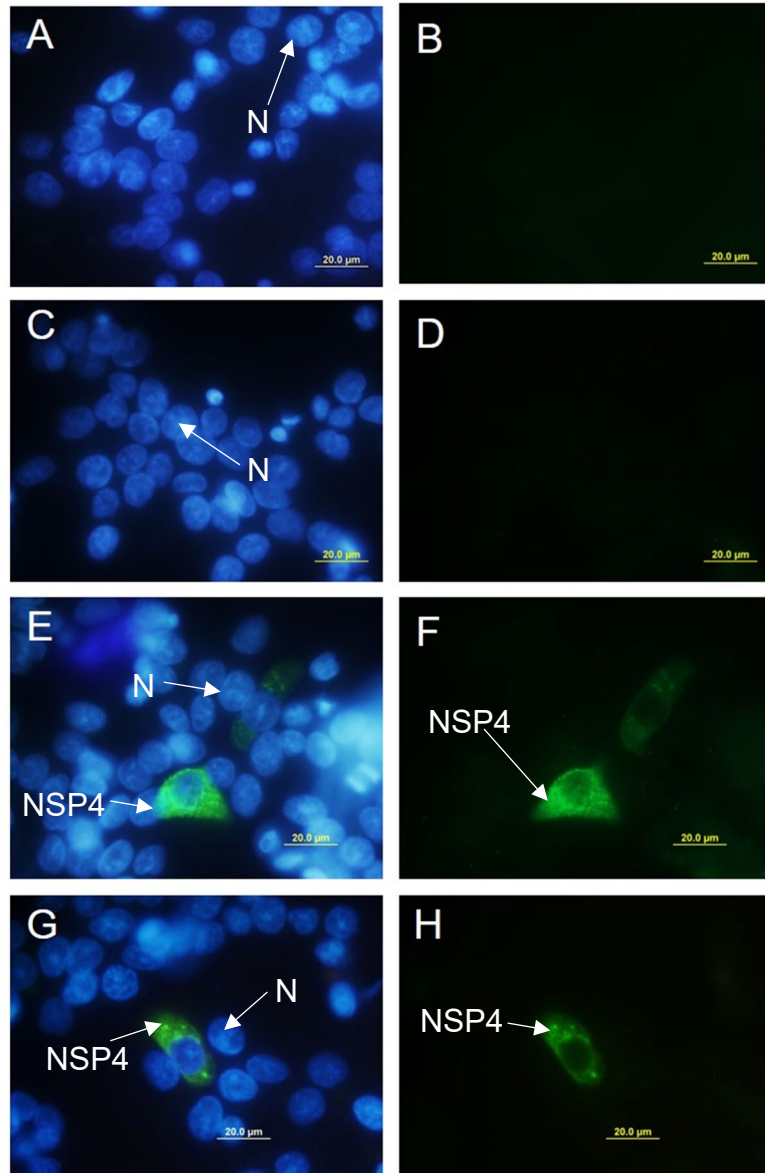


Figure 16. Detection of NSP4 in RV infected cells at 8 hpi. HT29.f8 cells were infected with RV at a MOI = 2 and treated with 20 $\mu$ M A3. At 8 hpi, the cells were fixed with 1% glutaraldehyde then fluorescently labeled with Hoechst 33342 dye which is selective for DNA (blue), and sequentially probed with polyclonal rabbit sera anti-NSP4<sub>150-175</sub> and Goat Anti-Rabbit IgG H&L (Alexa Fluor 488) to show the presence of NSP4 (green) A: NV treatment showed nuclei and no NSP4; B: NV treatment for NSP4 fluorescence only shows no NSP4; C: A3 treatment showed nuclei and no NSP4; D: A3 treatment for NSP4 fluorescence only shows no NSP4; E: RV treatment displayed nuclei with NSP4 (arrow) located within the cytoplasm; F: RV treatment for NSP4 fluorescence only shows NSP4 G: RV+A3 treatment displayed nuclei with NSP4 (arrow) within the cytoplasm; H: RV+A3 treatment for NSP4 fluorescence only shows NSP4. (X400)

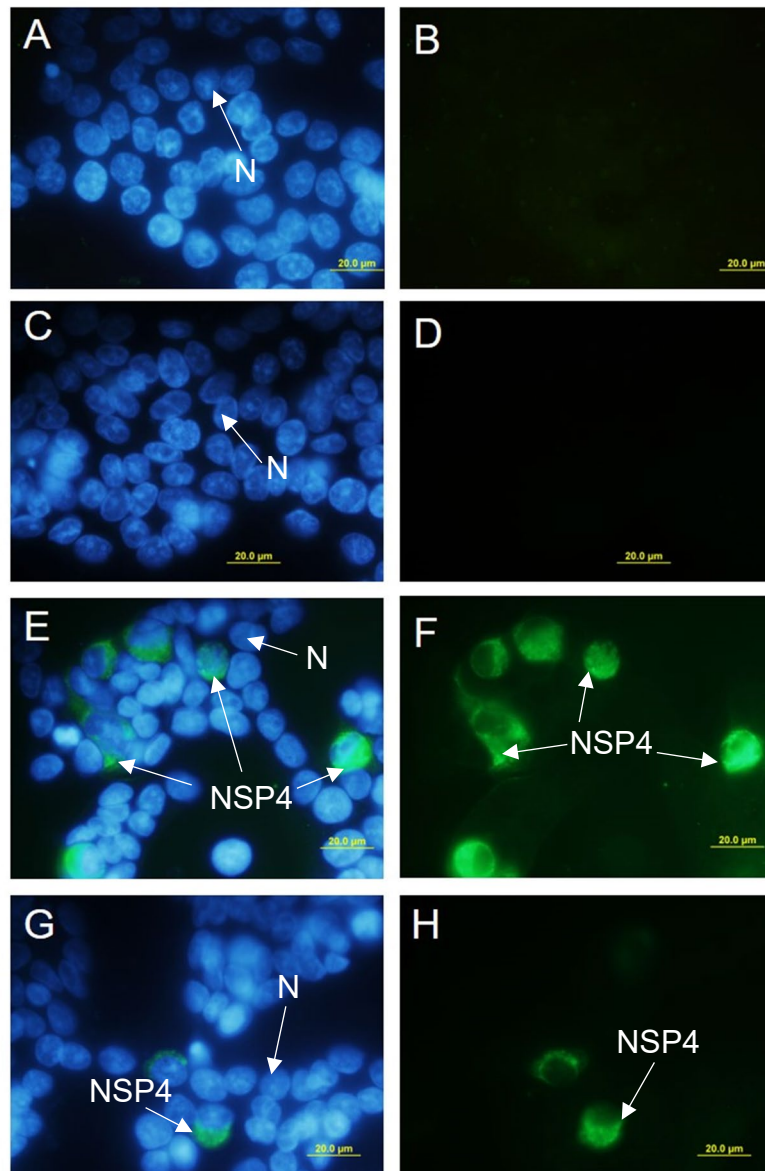


Figure 17. Detection of NSP4 in RV infected cells at 18 hpi. HT29.f8 cells were infected with RV at a MOI = 2 and treated with 20 $\mu$ M A3. At 18 hpi, the cells were fixed with 1% glutaraldehyde then fluorescently labeled with Hoechst 33342 dye which is selective for DNA (blue), and sequentially probed with polyclonal rabbit sera anti-NSP4<sub>150-175</sub> and Goat Anti-Rabbit IgG H&L (Alexa Fluor 488) to show the presence of NSP4 (green) A: NV treatment showed nuclei (N) and no NSP4; B: NV treatment for NSP4 fluorescence only shows no NSP4; C: A3 treatment showed nuclei and no NSP4; D: A3 treatment for NSP4 fluorescence only shows no NSP4; E: RV treatment displayed nuclei with NSP4 (arrow) located within the cytoplasm; F: RV treatment for NSP4 fluorescence only shows NSP4; G: RV+A3 treatment displayed nuclei with NSP4 (arrow) within the cytoplasm; H: RV+A3 treatment for NSP4 fluorescence only shows NSP4. (X400)

## Western Blot Analyses

To determine the expression and regulation of cellular proteins critical in lipid metabolism, cell lysates of HT29.f8 cells treated with NV, RV, RV+A3, and A3 collected at 12, 14, 16, and 18 hpi were probed with protein specific primary and goat anti-rabbit IgG Alexa Fluor® 546-labeled secondary antibodies.

To visualize the presence of perilipin 1 (PLIN1), rabbit anti-perilipin 1 and rabbit anti-GAPDH were used with 30 µg of cell lysate protein. The results showed a band at ~ 36 kDa for GAPDH and ~ 60 kDa for PLIN1 (Figure 18). The pixel densities for each band were quantified using ImagQuant software, then ratios of PLIN1 to GAPDH were calculated for normalization and graphed to quantify differences in protein expression (Figure 19).

The following antibodies were used in western blot assays to probe for their respective proteins, but no bands were observed (Table 5: Rabbit anti-TIP47, rabbit anti-ACAT, rabbit anti-DGAT1, mouse anti-DGAT, and mouse anti-ADRP).

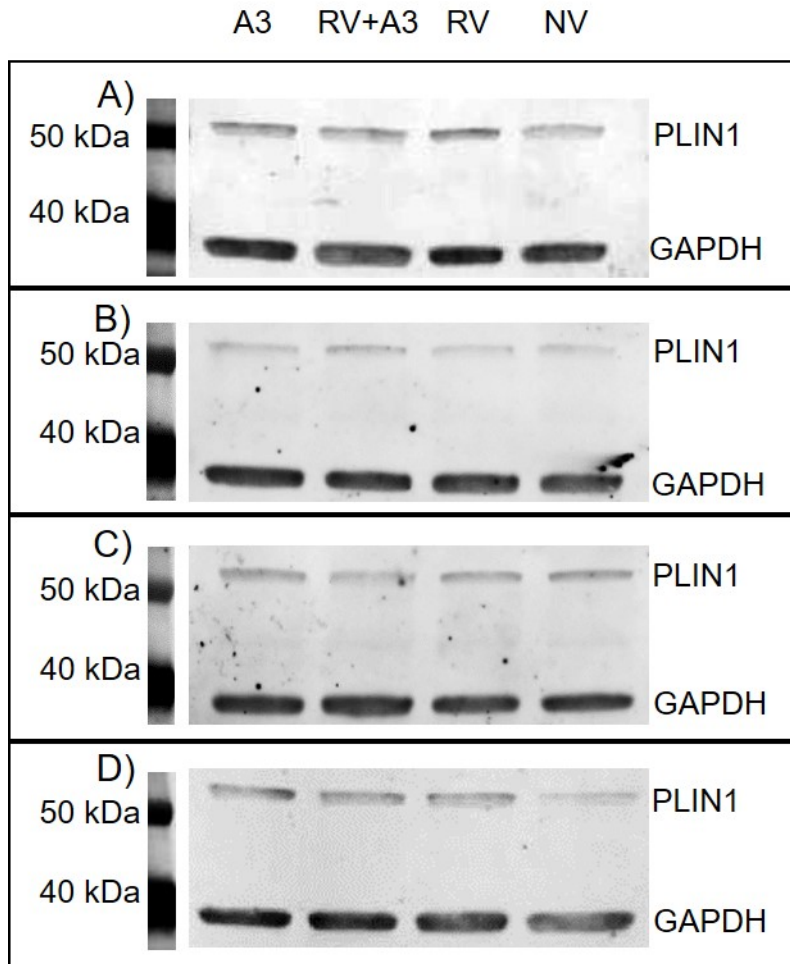


Figure 18. Time course study of the expression of Perilipin 1 (PLIN1) in RV infected HT29.f8 cells treated with A3. Western blot analysis on cell lysates (30  $\mu$ g) were separated on a 12% SDS/PAGE gel, electroblotted onto a nitrocellulose membrane and probed sequentially with 2  $\mu$ g/mL of rabbit anti-perilipin 1 and 40  $\mu$ g/mL goat anti-rabbit IgG Alexa Fluor® 546-labeled antibodies. Then GAPDH was visualized using 0.2  $\mu$ g/mL rabbit anti-GAPDH and 0.4  $\mu$ g/mL 40  $\mu$ g/mL goat anti-rabbit IgG Alexa Fluor® 546-labeled antibodies. The blots were visualized using the 556 nm excitation laser and 573 nm emission filter on the Typhoon 9500 plus laser scanner. A: 12 hpi; B: 14 hpi; C: 16 hpi; D: 18 hpi. Results showed a band at ~36 kDa for GAPDH and ~60 kDa for PLIN1.

## Ratios of Perilipin 1/GAPDH in HT29.f8 cells with treatments at 12, 14, 16, 18 hpi

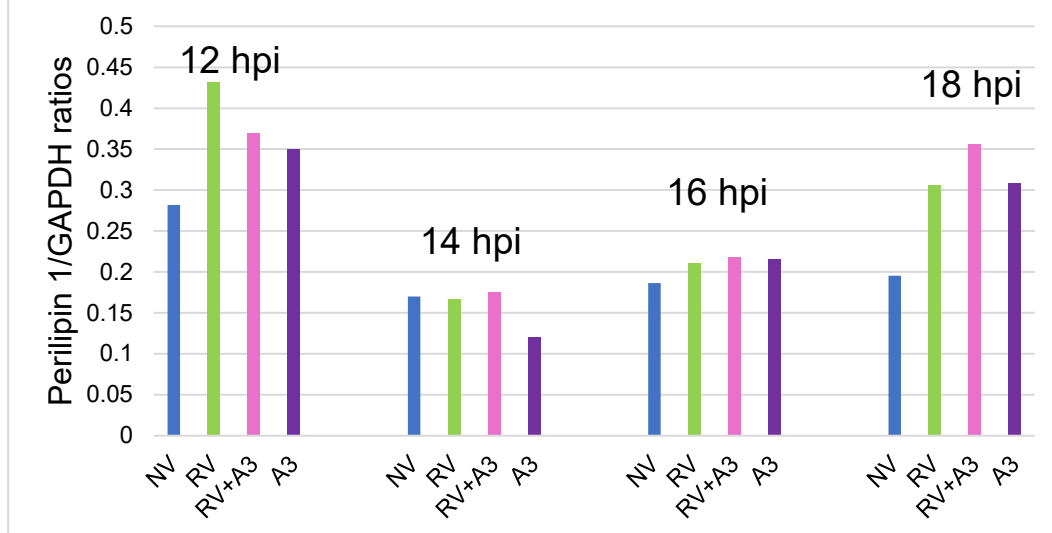


Figure 19. A time course study of the expression of perilipin 1 normalized to GAPDH. RV infected cells were treated with A3 and the control cells (NV and A3 alone) were collected at 12, 14, 16, 18 hpi. Western blot analysis was performed in duplicate experiments on cell lysates (30  $\mu$ g) separated on a 12% SDS/PAGE gel, electroblotted onto a nitrocellulose membrane and probed sequentially with 2  $\mu$ g/mL of rabbit anti-perilipin 1 and 40  $\mu$ g/mL goat anti-rabbit IgG Alexa Fluor® 546-labeled antibodies. Then GAPDH was visualized using 0.2  $\mu$ g/mL rabbit anti-GAPDH and 0.4  $\mu$ g/mL 40  $\mu$ g/mL goat anti-rabbit IgG Alexa Fluor® 546-labeled antibodies. The blots were visualized using the 556 nm excitation laser and 573 nm emission filter on the Typhoon 9500 plus laser scanner. Using ImaqQuant, the pixel densities for each band were obtained. The pixel density ratios for perilipin 1 to GAPDH were calculated and averaged for each treatment at each time point and graphed using Excel 2016. The ratio of perilipin/GAPDH at 12, 14, 16, and 18 hpi in NV treated cells (blue) was measured as 0.2816, 0.17, 0.1865 and 0.1954, respectively. The ratio of perilipin/GAPDH at 12, 14, 16, and 18 hpi in RV infected cells (green) demonstrated values of 0.4315, 0.167, 0.2105 and 0.3055, respectively. The ratio of perilipin/GAPDH at 12, 14, 16, and 18 hpi in RV+A3 treated cells (pink) showed values of 0.37, 0.1755, 0.2185 and 0.356, respectively. The ratio of perilipin/GAPDH at 12, 14, 16, and 18 hpi in A3 treated cells (purple) was measured as 0.3495, 0.1205, 0.215 and 0.308, respectively.

## **RT<sup>2</sup> Profiler PCR Array**

To determine the effects on cellular lipid metabolism when A3 is added to a RV infected human cells, the Human Lipoprotein Signaling and Cholesterol Metabolism RT<sup>2</sup> Profiler PCR Array was used to profile the expression of 84 key genes involved in lipoprotein transport and cholesterol metabolism. The experiments were performed using RNA extracted from HT29.f8 cells with NV, RV, RV+A3, and A3 treatments at 8 hpi. To verify that each experiment was performed properly, the RT<sup>2</sup> Profiler PCR Array also contained 5 housekeeping genes, a genomic DNA control, reverse transcription controls, and positive PCR controls. The housekeeping genes used were beta-actin (ACTB), beta-2-microglobulin (B2M), GAPDH, hypoxanthine phosphoribosyltransferase 1 (HPRT1), and ribosomal protein large P0 (RPLP0). However, a recent review has suggested that a minimum of two different housekeeping genes should be used for normalization of the data, and the Ct values should be similar between the genes as well as between all treatments (Kozera and Rapacz, 2013). Table 8 shows that the Ct values for ACTB, HPRT1 and RPLP0 were NV: 19.3318, 26.801, and 18.053; RV: 21.0134, 27.6561, and 19.1568; RV+A3: 20.8755, 26.7172, and 18.2995; A3: 20.0768, 26.2385, and 17.7653, respectively. The Ct values for B2M (NV 22.4365, RV 23.3247, RV+A3 22.3989, and A3 21.9764) and GAPDH (NV 21.0012, RV 22.6052, RV+A3 22.1545, and A3 21.3463) were similar to each other as well as between the treatments, therefore the data analysis was performed using these two housekeeping genes (Table 8).

To ensure there was no genomic DNA contamination in the RNA sample prior to reverse transcription, a genomic DNA control was used in each sample during each run. The Ct value for the genomic DNA control should be greater than 35 to show no genomic DNA contamination; moreover, the Ct value for NV, RV, RV+A3, and A3 were 38.3939, 40.3818, 38.3315, and 39.0001, respectively. The reverse transcription control (RTC) was performed in triplicate for each sample during each run to check for RNA quality. The Ct value for the reverse transcription control is expected to be  $20 \pm 2$ ; likewise, the Ct value for all treatments among the plates were as follows: NV 21.8052, 21.7841, and 21.5926; RV 21.2644, 21.216, and 21.592; RV+A3 21.177, 21.2524, and 21.5495; A3 21.0988, 21.1118, and 21.4397 (Table 8). The positive PCR controls (PPC) were performed in triplicate for each sample during each run to test the efficiency of the PCR reaction itself. The Ct value for the positive PCR control is expected to be  $20 \pm 2$ ; likewise, the Ct value for all treatments among the plates were as follows: NV 19.799, 19.6583, and 19.8622 ; RV 19.8231, 19.7214, and 19.8572; RV+A3 19.906, 19.7779, and 19.9912; A3 19.6843, 19.6357, and 19.6077 (Table 8). To detect for the presence of reverse transcription inhibitors, the  $\Delta\text{Ct}$  RTC was calculated using the following equation:

$$\Delta\text{Ct} = \text{AVG Ct}^{\text{RTC}} - \text{AVG Ct}^{\text{PPC}}$$

If no inhibition of the reverse transcription reaction was apparent, the  $\Delta\text{Ct}$  RTC should be less than five; furthermore, the  $\Delta\text{Ct}$  RTC for NV, RV, RV+A3, and A3 were 1.95417, 1.55693, 1.4342, and 1.57356, respectively (Table 8).

Table 8. RT<sup>2</sup> Profiler PCR Array controls.

	Genes	NV	RV	RV+A3	A3
Housekeeping genes <sup>a</sup>	ACTB	19.3318	21.0134	20.8755	20.0768
	B2M	22.4365	23.3247	22.3989	21.9764
	GAPDH	21.0012	22.6052	22.1545	21.3463
	HPRT	26.801	27.6561	26.7172	26.2385
	RPLP0	18.053	19.1568	18.2995	17.7653
Genomic DNA Control <sup>b</sup>	HGDC	38.3939	40.3818	38.3315	39.0001
Reverse Transcription Controls <sup>c</sup>	RTC	21.8052	21.2644	21.177	21.0988
	RTC	21.7841	21.216	21.2524	21.1118
	RTC	21.5926	21.592	21.5495	21.4379
Positive PCR Controls <sup>d</sup>	PPC	19.799	19.8231	19.906	19.6843
	PPC	19.6583	19.7214	19.779	19.6357
	PPC	19.8622	19.8572	19.9912	19.6077
$\Delta$ Ct RTC <sup>e</sup>		1.95417	1.55693	1.4342	1.57356

a – Data normalization

b - To detect genomic DNA contamination

c – Reverse Transcription control is to check for RNA sample quality

d – Positive PCR control is to test for the PCR reaction itself

e – To detect inhibitors for reverse transcription

The fold-changes (FC) for each of the 84 genes were calculated and 15 genes showed a >1.5 fold change (up or down regulation) with at least one treatment (appendix) (Table 9). Interestingly, the only gene found to be significantly down-regulated in RV infected HT29.f8 cells was CELA3B (0.4155). The genes found to be up-regulated in RV infected cells were ANGPLT3, APOA1, APOB, CYP39A1, LCAT, and LRP12 (1.9973, 1.6756, 2.791, 1.7701, 1.5557, and 1.8157, respectively). The only gene found to be up-regulated in RV+A3 treated cells was APOF (1.719). The genes found to be down-regulated in RV+A3 treated cells were ANGPLT3, APOA1, APOA4, CELA3B, SCARF1, and STAB2 (0.2505, 0.313, 0.3719, 0.4843, 0.4115, and 0.389, respectively). No genes were found to be significantly down-regulated by A3 treated cells; however, APOF, CELA3A, CETP, COLEC12, and IL4 were calculated to be up-regulated (1.6273, 1.6769, 13.858, 5466.1, and 2.7431, respectively)

Intriguingly, five genes (ANGPLT3, APOA1, CYP39A1, LRP12, and OSBPL1A) showed similar expression patterns among the treatments: RV, RV+A3, and A3. These five genes showed an up-regulation with RV treatment, down-regulation with RV+A3, and a slight down-regulation with A3 (Figure 20).

Table 9. Genes that showed a >1.5 fold in up or down regulation from the RT<sup>2</sup> Profiler PCR Array

Gene	RV	RV+A3	A3
ANGPLT3	1.9973	0.2505	0.8406
APOA1	1.6756	0.313	0.805
APOA4	1.4271	0.3719	0.7728
APOB	2.791		
APOF	1.2642	1.719	1.6273
CELA3A	1.2962	1.1895	1.6769
CELA3B	0.4155	0.4843	
CETP			13.858
COLEC12			5466.1
CYP39A1	1.7701	0.9603	1.1096
IL4			2.7431
LCAT	1.5557	0.8406	0.7566
LRP12	1.8157	0.9526	0.9653
SCARF1	0.8137	0.4115	0.8192
STAB2		0.389	1.0157

Pink highlight >1.5 fold up-regulation  
 Green highlight >1.5 fold down-regulation

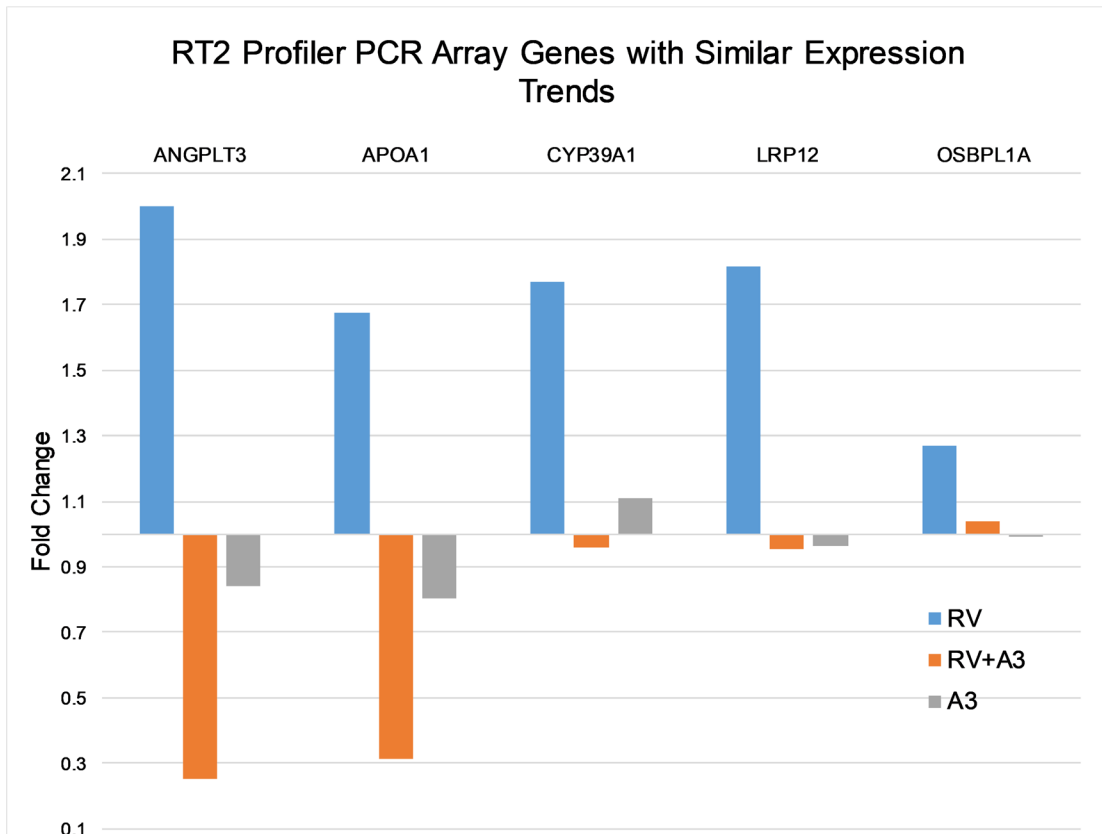


Figure 20. Differential expression of key genes in lipoprotein signaling and cholesterol metabolism pathways. HT29.f8 cells were infected with RV – Wa (MOI = 2) or mock-infected and treated with A3 for 1 h at 37°C. Total RNA was isolated from the cells treated with NV, RV, RV + 20 μM A3, or 20 μM A3 at 8 hpi. mRNA levels were measured by quantitative real-time RT-PCR assay using the RT<sup>2</sup> Profiler PCR Array. The levels of glyceraldehyde-3-phosphate dehydrogenase (GAPDH) and beta-3-microglobulin (B2M) were used to normalize the quantities of target mRNA. Fold changes in signals of expression of the gene of interest relative to GAPDH and B2M were calculated using the Livak method ( $2^{-\Delta\Delta Ct}$ ). RV infections alone (blue) showed an upregulation in the following genes: ANGPLT3, APOA1, CYP39A1, LRP12 and OSBPL1A with fold changes of 1.997, 1.676, 1.77, 1.816, and 1.269, respectively. RV+A3 treatments (orange) displayed downregulations in the following genes: ANGPLT3, APOA1, CYP39A1, and LRP12 with fold changes of 0.25, 0.313, 0.96, and 0.963, respectively; however, a slight up-regulation was observed in OSBPL1A with the fold change of 1.041. A3 treatments (gray) exhibited downregulations in the following genes: ANGPLT3, APOA1, LRP12 and OSBPL1A with fold changes of 0.841, 0.805, 0.965, and 0.989, respectively; however, a slight up-regulation was observed in CYP39A1 with the fold change of 1.11.

## DISCUSSION

RV infections alter many cellular metabolic pathways including lipid metabolism (Gaunt et al., 2013; Lever and Desselberger, 2016; Mohan et al., 2008). Correspondingly, several other studies show RV replication and assembly is dependent on cholesterol and CLD (Gaunt et al., 2013; Lever and Desselberger, 2016; Mohan et al., 2008). The hypothesis of this study was that the regulation of lipid metabolism in RV infected HT29.f8 cells would be affected by A3 treatment. Experiments were designed using qRT-PCR, western blots, histochemical and fluorescence microscopy to examine changes in cellular transcripts, proteins, and neutral fats found in CLDs in RV infected HT29.f8 cells with/without A3.

The optimization of cDNA for qRT-PCR assays demonstrated that the loss of cDNA using the two purification kits, as outlined above, resulted in a significant difference in the production of primer specific amplicons. This implies that a loss of cDNA that represents the transcripts of low abundance may cause a misrepresentation of gene expression. Therefore, unprocessed cDNA was used for a more authentic representation of the gene expression profile.

There is no published data on the transcriptional regulation of lipid metabolism genes in RV infected cells treated with A3. Therefore, the data from this study is very important in defining specific genes that are involved in the

control of lipids in the cell as well as suggesting mechanisms of action of A3. The fact that the expression of ETKN1 showed little to no regulation across all treatments suggests that an alteration in the lipid pathway is downstream of this gene. ETKN1 is the first dedicated step in the conversion of ethanolamine to phosphatidylethanolamine (PE), but it is not the rate-limiting step (Gibellini and Smith, 2010; Lykidis et al., 2001). Once PE is made there are several known pathways in which PE has a major role in lipid trafficking and membrane integrity (Gibellini and Smith, 2010; Lykidis et al., 2001). Further experiments should be performed to see if these other pathways are affected.

The expression of HMGCR is the rate-limiting step in the production of *de novo* cholesterol (Goldstein and Brown, 2009). The up-regulation of HMGCR in RV infected cells implies that RV manipulates cholesterol metabolism through the HMGCR pathway, which would increase cholesterol production. Interestingly, a decrease in HMGCR was observed with the addition of A3, which implies that the expression of HMGCR transcripts was targeted by an unknown mechanism of action.

Unexpectedly, LDLR expression was also significantly increased in RV infected cells. Usually, LDLR and HMGCR are activated simultaneously, which results in a negative feedback loop that regulates the uptake and synthesis of cholesterol. This results in the increase in one of the two genes (HMGCR and LDLR) while the other is down-regulated. This data indicates that RV alters the normal cellular negative feedback loop that controls the amount of cholesterol in

the cell. The significant decrease in LDLR expression observed with A3 treatment indicates the importance in the regulation of LDLR for cellular homeostasis.

Another key gene, Perilipin 4, is important for protecting the CLDs from breakdown by hormone-sensitive lipases; therefore, the decrease in expression induced by RV infection implies that the neutral fats within the CLD were metabolized for energy (Sun et al., 2013). The additional treatment with A3 did not significantly change the expression pattern observed with RV alone, and the addition of A3 treatment by itself caused a less significant change in expression. Further experiments need to be designed to elucidate the mechanism of actions of A3 on Perilipin 4 expression.

Another member of the perilipin family of proteins, PLIN1, which protects CLDs from breaking down by hormone-sensitive lipases and promotes lipid droplet enlargement, was examined using a western blot time course analysis. The increase in PLIN1 protein expression observed at 12 and 18 hpi indicates that CLDs are being produced by the cell for further energy use; however, at 14 and 16 hpi PLIN1 protein expression decreased, suggesting the CLDs are being broken down for energy use. (Grahn et al., 2013). Overall, this implies a cycling pattern for the production and break down of CLDs. However, this study needs to be performed in triplicate and future studies are needed to determine time dependent regulation.

The differential histochemical staining for neutral fats revealed that A3 is modulating lipid metabolism. In support of this observation, using a fluorescently labeled stain for CLDs, PM, and nuclei, showed the modulation of lipid metabolism and PM integrity by the addition of A3 to RV infected cells.

The RT<sup>2</sup> Profiler PCR array assays demonstrated that of the 84 genes tested, only 15 showed >1.5 fold change. This illustrated that lipid metabolism is regulated with at least one of three treatments tested (RV, RV+A3, or A3). However, validation of the results for LRP12, IL4, COLEC12, CETP, and ANGPT3 using in-house designed gene specific primer sets failed to produce visible amplicons. The RT<sup>2</sup> Profiler PCR array was optimized for high sensitivity for transcripts in low expression, but the specificity may have decreased. Therefore, further studies will need to be performed to optimize the qRT-PCR experimental set up for high sensitivity while keeping high specificity.

Altogether, this study showed that the treatment of RV+A3 caused a modification of the gene regulation and alter the accumulation and distribution of neutral fats. Additionally, RV+A3 treatment showed an improvement in PM integrity when compared to RV alone. The transcripts involved in lipoprotein signaling and cholesterol metabolism appeared to occur in low frequency at 8 hpi; therefore, the highly sensitive assay, RT<sup>2</sup> Profiler PCR Array, was able to detect the changes, whereas the designed primer sets with high specificity could not. This infers that an earlier time point of ~1 – 2 hpi would be appropriate to repeat the RT<sup>2</sup> Profiler PCR Array experiments. This time point might be crucial

due to the importance of cholesterol and CLDs in the production of the viroplasm which is shown to form as early as ~1 – 2 hpi (Carrão-Torres et al., 2010; Eichwald et al., 2012). This study has presented data that will help discern the mechanism of action of A3 on RV infected cells and has the potential to develop a universal therapeutic treatment for RV infections.

## References

- Abou-nader, A.J., Sauer, M.A., Steele, A.D., Tate, J.E., Atherly, D., Parashar, U.D., Santosham, M., Anthony, E.S., Sauer, M.A., Steele, A.D., Jacqueline, E., Atherly, D., Parashar, U.D., Santosham, M., Nelson, E.A.S., 2018. Global rotavirus vaccine introductions and coverage : 2006 – 2016. *Hum. Vaccin. Immunother.* 14, 2218–2296.  
<https://doi.org/10.1080/21645515.2018.1470725>
- Acharya, N., Penukonda, S., Shcheglova, T., Hagymasi, A.T., Basu, S., Srivastava, P.K., 2017. Endocannabinoid system acts as a regulator of immune homeostasis in the gut. *Proc. Natl. Acad. Sci.* 114, 5005–5010.  
<https://doi.org/10.1073/pnas.1612177114>
- Aggarwal, B.B., Bhardwaj, A., Aggarwal, R.S., Seeram, N.P., Shishodia, S., Takada, Y., 2004. Role of resveratrol in prevention and therapy of cancer: Preclinical and clinical studies, in: *Anticancer Research*. pp. 2783–2840.
- Alkali, B.R., Daneji, A.I., Magaji, A.A., Bilbis, L.S., 2015. Clinical Symptoms of Human Rotavirus Infection Observed in Children in Sokoto, Nigeria. *Adv. Virol.* Volume 201. <https://doi.org/10.1155/2015/890957>
- Alphonse, P.A.S., Jones, P.J.H., 2016. Revisiting Human Cholesterol Synthesis and Absorption: The Reciprocity Paradigm and its Key Regulators. *Lipids* 51, 519–536. <https://doi.org/10.1007/s11745-015-4096-7>
- Annis, D.S., Mosher, D.F., Roberts, D.D., 2009. Chronic Rotavirus Infection in an Infant with Severe Combined Immunodeficiency: Successful Treatment by Hematopoietic Stem Cell Transplantation. *Clin Immunol.* 27, 339–351.  
<https://doi.org/10.1016/j.neuron.2009.10.017.A>
- Aoki, S.T., Settembre, E., Trask, S.D., Greenberg, H.B., Stephen, C., Dormitzer, P.R., 2010. Structure of rotavirus outer-layer protein VP7 bound with a neutralizing Fab. *Science* (80- ). 324, 1444–1447.  
<https://doi.org/10.1126/science.1170481.Structure>
- Arias, C.F., Silva-Ayala, D., López, S., 2015. Rotavirus Entry: a Deep Journey into the Cell with Several Exits. *J. Virol.* 89, 890–893.  
<https://doi.org/10.1128/JVI.01787-14>
- Arnold, M., Patton, J.T., McDonald, S.M., 2012. Culturing, Storage and Quantification of Rotaviruses. *Curr Protoc Microbiol* 1–29.  
<https://doi.org/10.1002/9780471729259.mc15c03s15.Culturing>

- Asano, L., Watanabe, M., Ryoden, Y., Usuda, K., Yamaguchi, T., Khambu, B., Takashima, M., Sato, S. ichi, Sakai, J., Nagasawa, K., Uesugi, M., 2017. Vitamin D Metabolite, 25-Hydroxyvitamin D, Regulates Lipid Metabolism by Inducing Degradation of SREBP/SCAP. *Cell Chem. Biol.* 24, 207–217. <https://doi.org/10.1016/j.chembiol.2016.12.017>
- Athar, M., Back, J.H., Tang, X., Kopelovich, L., Bickers, D., Kim, A., 2009. Resveratrol: A Review of Pre-Clinical Studies for Human Cancer Prevention. *Toxicol Appl Pharmacol* 43, 1698–1710. <https://doi.org/10.1016/j.paid.2007.05.007>. Dispositional
- Auclair, N., Melbouci, L., St-pierre, D., Levy, E., 2017. Gastrointestinal factors regulating lipid droplet formation in the intestine. *Exp. Cell Res.* <https://doi.org/10.1016/j.yexcr.2017.12.031>
- Ball, J.M., Medina-Bolivar, F., Defrates, K., Hambleton, E., Hurlburt, M.E., Fang, L., Yang, T., Nopo-Olazabal, L., Atwill, R.L., Ghai, P., Parr, R.D., 2015. Investigation of Stilbenoids as Potential Therapeutic Agents for Rotavirus Gastroenteritis. *Adv. Virol.* 2015. <https://doi.org/10.1155/2015/293524>
- Beilstein, F., Carrière, V., Leturque, A., Demignot, S., 2016. Characteristics and functions of lipid droplets and associated proteins in enterocytes. *Exp. Cell Res.* 340, 172–179. <https://doi.org/10.1016/j.yexcr.2015.09.018>
- Bennett, R.N., Wallsgrove, R.M., 1994. Tansley review no. 72. Secondary metabolites in plant defence mechanisms. *New Phytol.* 127, 617–633.
- Bhandari, N., Rongsen-Chandola, T., Bavdekar, A., John, J., Antony, K., Taneja, S., Goyal, N., Kawade, A., Kang, G., Rathore, S.S., Juvekar, S., Muliyl, J., Arya, A., Shaikh, H., Abraham, V., Vрати, S., Proschan, M., Kohberger, R., Thiry, G., Glass, R., Greenberg, H.B., Curlin, G., Mohan, K., Harshavardhan, G.V.J.A., Prasad, S., Rao, T.S., Boslego, J., Bhan, M.K., 2014. Efficacy of a monovalent human-bovine (116E) rotavirus vaccine in Indian infants: A randomised, double-blind, placebo-controlled trial. *Lancet* 383, 2136–2143. [https://doi.org/10.1016/S0140-6736\(13\)62630-6](https://doi.org/10.1016/S0140-6736(13)62630-6)
- Bishop, R., Davidson, G.P., Holmes, I.H., Ruck, B.J., 1973. Virus Particles in Epithelial Cells of Duodenal Mucosa from Children with Acute Non-bacterial Gastroenteritis. *Lancet* 302, 1281–1283. [https://doi.org/10.1016/S0140-6736\(73\)92867-5](https://doi.org/10.1016/S0140-6736(73)92867-5)

- Brents, L.K., Medina-Bolivar, F., Seely, K. a., Nair, V., Bratton, S.M., Ñopo-Olazabal, L., Patel, R.Y., Liu, H., Doerksen, R.J., Prather, P.L., Radomska-Pandya, A., Nopo-Olazabal, L., Patel, R.Y., Liu, H., Doerksen, R.J., Prather, P.L., Radomska-Pandya, A., Ñopo-Olazabal, L., Huang, C.-P., Au, L.-C., Chiou, R.Y.-Y., Chung, P.-C., Chen, S.-Y., Tang, W.-C., Chang, C.-L., Fang, W.-H., Lin, S.-B., 2012. Natural prenylated resveratrol analogs arachidin-1 and -3 demonstrate improved glucuronidation profiles and have affinity for cannabinoid receptors. *Xenobiotica*. 42, 139–156.  
<https://doi.org/10.3109/00498254.2011.609570>
- Caillot, D., Escoffre, M., Arnulf, B., Macro, M., Belhadj, K., Garderet, L., Roussel, M., Payen, C., Mathiot, C., Femand, J.P., Meuleman, N., Rollet, S., Maglio, M.E., Zeytoonjian, A.A., Weller, E.A., Ph, D., Munshi, N., Anderson, K.C., Richardson, P.G., Facon, T., Loiseau, H.A., Harousseau, J.L., Moreau, P., Study, I.F.M., 2006. Safety and Efficacy of an Attenuated Vaccine against Severe Rotavirus Gastroenteritis. *N. Engl. J. Med.* 354, 1311–1320.  
<https://doi.org/10.1056/NEJMoa1611750>
- Carrão-Torres, J.J., Gutiérrez, M., Arias, C.F., Lápez, S., Isa, P., 2010. Characterization of viroplasm formation during the early stages of rotavirus infection. *Virol. J.* 7, 1–11. <https://doi.org/10.1186/1743-422X-7-350>
- Changotra, H., 2017. Rotavirus virus - like particles ( RV - VLPs ) vaccines : An update. *Rev. Med Virol.* e1954. <https://doi.org/10.1002/rmv.1954>
- Cheung, W., Gill, M., Esposito, A., Kaminski, C.F., Courousse, N., Chwetzoff, S., Trugnan, G., Keshavan, N., Lever, A., Desselberger, U., 2010. Rotaviruses Associate with Cellular Lipid Droplet Components To Replicate in Viroplasms, and Compounds Disrupting or Blocking Lipid Droplets Inhibit Viroplasm Formation and Viral Replication. *J. Virol.* 84, 6782–6798.  
<https://doi.org/10.1128/JVI.01757-09>
- Clark, A., Black, R., Tate, J., Roose, A., Kotloff, K., Lam, D., Blackwelder, W., Parashar, U., Lanata, C., Kang, G., Troeger, C., Platts-Mills, J., Mokdad, A., Global Rotavirus Surveillance Network, G.R.S., Sanderson, C., Lamberti, L., Levine, M., Santosham, M., Steele, D., 2017. Estimating global, regional and national rotavirus deaths in children aged. *PLoS One* 12, e0183392.  
<https://doi.org/https://doi.org/10.1371/journal.pone.0183392>
- Cohen, J., Laporte, J., Charpilienne, A., Scherrer, R., 1979. Activation of rotavirus RNA polymerase by calcium chelation. *Arch. Virol.* 60, 177–186.  
<https://doi.org/10.1007/BF01317489>
- Crawford, S.E., Mukherjee, S.K., Estes, M.K., Lawton, J.A., Shaw, A.L., Ramig, R.F., Prasad, B. V, 2001. Trypsin cleavage stabilizes the rotavirus VP4 spike. *J. Virol.* 75, 6052–61. <https://doi.org/10.1128/JVI.75.13.6052-6061.2001>

- Crawford, S.E., Ramani, S., Tate, J.E., Parashar, U.D., Svensson, L., Hagbom, M., Franco, M.A., Greenberg, H.B., O’Ryan, M., Kang, G., Desselberger, U., Estes, M.K., 2017. Rotavirus infection. *Nat. Rev. Dis. Prim.* 3. <https://doi.org/10.1038/nrdp.2017.83>
- Criglar, J.M., Anish, R., Hu, L., Crawford, S.E., Sankaran, B., 2018. Phosphorylation cascade regulates the formation and maturation of rotaviral replication factories. *PNAS* 115, e12015–e12023. <https://doi.org/10.1073/pnas.1717944115>
- Davidson, N.O., 2018. Genetic Regulation of Intestinal Lipid Transport and Metabolism, Sixth Edit. ed, *Physiology of the Gastrointestinal Tract: Sixth Edition*. Elsevier Inc. <https://doi.org/10.1016/B978-0-12-809954-4.00049-9>
- Deen, J., Lopez, A.L., Kanungo, S., Wang, X.Y., Anh, D.D., Tapia, M., Grais, R.F., 2018. Improving rotavirus vaccine coverage: Can newer-generation and locally produced vaccines help? *Hum. Vaccines Immunother.* 14, 495–499. <https://doi.org/10.1080/21645515.2017.1403705>
- Degirolamo, C., Sabbà, C., Moschetta, A., 2015. Intestinal nuclear receptors in HDL cholesterol metabolism. *J. Lipid Res.* 56, 1262–1270. <https://doi.org/10.1194/jlr.r052704>
- Demignot, S., Beilstein, F., Morel, E., 2013. Triglyceride-rich lipoproteins and cytosolic lipid droplets in enterocytes : Key players in intestinal physiology and metabolic disorders *Biochimie Triglyceride-rich lipoproteins and cytosolic lipid droplets in enterocytes : Key players in intestinal phys. Biochimie* 1–8. <https://doi.org/10.1016/j.biochi.2013.07.009>
- Desselberger, U., 2014. Rotaviruses. *Virus Res.* 190, 75–96. <https://doi.org/10.1016/j.virusres.2014.06.016>
- Devane, W.A., Dysarz, F.A., Johnson, M.R., Melvin, L.S., Howlett, A.C., 1988. Determination and characterization of a cannabinoid receptor in rat brain. *Mol. Pharmacol.* 34, 605–13.
- Di Marzo, V., Izzo, A.A., 2006. Endocannabinoid overactivity and intestinal inflammation. *Gut* 55, 1373–1376. <https://doi.org/10.1136/gut.2005.090472>
- Eichwald, C., Arnoldi, F., Laimbacher, A.S., Schraner, E.M., Fraefel, C., Wild, P., Burrone, O.R., Ackermann, M., 2012. Rotavirus Viroplasm Fusion and Perinuclear Localization Are Dynamic Processes Requiring Stabilized Microtubules. *PLoS One* 7. <https://doi.org/10.1371/journal.pone.0047947>
- Engelking, L.J., McFarlane, M.R., Li, C.K., Liang, G., 2012. Blockade of cholesterol absorption by ezetimibe reveals a complex homeostatic network in enterocytes. *J. Lipid Res.* 53, 1359–1368. <https://doi.org/10.1194/jlr.m027599>

- Estes, M.K., Kapikian, A.Z., 2007. Rotaviruses and Their Replication, in: Knipe DM, Howley PM (Eds). *Fields Virology*. Lippincott Williams, Philadelphia, pp. 1917–1974.
- Fernández De Castro, I., Tenorio, R., Risco, C., 2016. Virus assembly factories in a lipid world. *Curr. Opin. Virol.* 18, 20–26.  
<https://doi.org/10.1016/j.coviro.2016.02.009>
- Gambini, J., Inglés, M., Olaso, G., Lopez-Grueso, R., Bonet-Costa, V., Gimeno-Mallench, L., Mas-Bargues, C., Abdelaziz, K.M., Gomez-Cabrera, M.C., Vina, J., Borrás, C., 2015. Properties of Resveratrol: In Vitro and In Vivo Studies about Metabolism, Bioavailability, and Biological Effects in Animal Models and Humans. *Oxid. Med. Cell. Longev.* 2015, 1–13.  
<https://doi.org/10.1155/2015/837042>
- Gaunt, E.R., Zhang, Q., Cheung, W., Wakelam, M.J.O., Lever, A.M.L., Desselberger, U., 2013. Lipidome analysis of rotavirus-infected cells confirms the close interaction of lipid droplets with viroplasm. *J. Gen. Virol.* 94, 1576–1586. <https://doi.org/10.1099/vir.0.049635-0>
- Gibellini, F., Smith, T.K., 2010. The Kennedy pathway-de novo synthesis of phosphatidylethanolamine and phosphatidylcholine. *IUBMB Life* 62, 414–428. <https://doi.org/10.1002/iub.337>
- Goldstein, J.L., Brown, M.S., 2009. History of Discovery : The LDL Receptor. *Arterioscler. Thromb.* 29, 431–438.  
<https://doi.org/10.1161/ATVBAHA.108.179564.History>
- Grahn, T.H.M., Zhang, Y., Lee, M.-J., Sommer, A.G., Mostoslavsky, G., Fied, S.F., Greenburg, A.S., Puri, V., 2013. FSP27 and PLIN1 interaction promotes the formation of large lipid droplets in human adipocytes. *Biochem Biophys Res Commun.* 432, 296–301.  
<https://doi.org/10.1016/j.bbrc.2013.01.113>
- Hasenoehrl, C., Taschler, U., Storr, M., Schicho, R., 2016. The gastrointestinal tract – a central organ of cannabinoid signaling in health and disease. *Neurogastroenterol. Motil.* 28, 1765–1780.  
<https://doi.org/10.1111/nmo.12931>
- Heller, S., Cable, C., Penrose, H., Makboul, R., Biswas, D., Cabe, M., Crawford, S.E., Savkovic, S.D., 2016. Intestinal inflammation requires FOXO3 and prostaglandin E2-dependent lipogenesis and elevated lipid droplets. *Am. J. Physiol. Liver Physiol.* 310, G844–G854.  
<https://doi.org/10.1152/ajpgi.00407.2015>
- Henne, W.M., Reese, M.L., Goodman, J.M., 2018. The assembly of lipid droplets and their roles in challenged cells. *EMBO J.* e98947.  
<https://doi.org/10.15252/embj.201898947>

- Holloway, G., Coulson, B.S., 2013. Innate cellular responses to rotavirus infection. *J. Gen. Virol.* 94, 1151–1160. <https://doi.org/10.1099/vir.0.051276-0>
- Huang, C.-P., Au, L.-C., Chiou, R.Y.-Y., Chung, P.-C., Chen, S.-Y., Tang, W.-C., Chang, C.-L., Fang, W.-H., Lin, S.-B., 2010. Arachidin-1, a Peanut Stilbenoid, Induces Programmed Cell Death in Human Leukemia HL-60 Cells. *J. Agric. Food Chem.* 12123–12129. <https://doi.org/10.1021/jf102993j>
- Hussain, M.M., 2009. Intestinal Lipid Absorption and Lipoprotein Formation. *Curr Opin Lipidol* 49, 1841–1850. <https://doi.org/10.1097/MOL.0000000000000084>
- Izzo, A.A., Camilleri, M., 2008. Emerging role of cannabinoids in gastrointestinal and liver diseases: basic and clinical aspects. *Gut* 57, 1140–1155. <https://doi.org/10.1136/gut.2008.148791>
- Jayaram, H., Estes, M.K., Prasad, B.V.V., 2004. Emerging themes in rotavirus cell entry, genome organization, transcription and replication. *Virus Res.* 101, 67–81. <https://doi.org/https://doi.org/10.1016/j.virusres.2003.12.007>
- Jiang, V., Jiang, B., Tate, J., Parashar, U.D., Patel, M.M., 2010. Performance of rotavirus vaccines in developed and developing countries. *Hum. Vaccin.* 6, 532–542. <https://doi.org/10.4161/hv.6.7.11278>
- Khalid, Y., Andersson, M., Hagbom, M., Novak, D., Ekstro, M., 2017. Ondansetron treatment reduces rotavirus symptoms — A randomized double-blinded. *PLoS One* 12, e0186824. <https://doi.org/https://doi.org/10.1371/journal.pone.0.186824>
- Khodabandehloo, M., Shamsi Shahrabadi, M., Keyvani, H., Bambai, B., Sadigh, Z.A., 2012. Recombinant outer capsid glycoprotein (VP7) of rotavirus expressed in insect cells induces neutralizing antibodies in rabbits. *Iran. J. Public Health* 41, 73–84.
- Kozera, B., Rapacz, M., 2013. Reference genes in real-time PCR. *J. Appl. Genet.* 54, 391–406. <https://doi.org/10.1007/s13353-013-0173-x>
- Kriaa, A., Bourgin, M., Potiron, A., Mkaouar, H., Jablaoui, A., Gérard, P., Maguin, E., Rhimi, M., 2019. Microbial impact on cholesterol and bile acid metabolism: current status and future prospects. *J. Lipid Res.* 60, 323–332. <https://doi.org/10.1194/jlr.r088989>
- Lawton, J.A., Estes, M.K., Prasad, B.V.V., 1997. Three-dimensional visualization of mRNA release from actively transcribing rotavirus particles. *Nat. Struct. Biol.* 4, 118–121. <https://doi.org/doi:10.1038/nsb0297-118>

- Lee, L.Y., Ison, M.G., 2014. Diarrhea caused by viruses in transplant recipients. *Transpl. Infect. Dis.* 16, 347–358. <https://doi.org/10.1111/tid.12212>
- Lever, A., Desselberger, U., 2016. Rotavirus replication and the role of cellular lipid droplets: New therapeutic targets? *J. Formos. Med. Assoc.* 115, 389–394. <https://doi.org/10.1016/j.jfma.2016.02.004>
- Li, Z., Baker, M.L., Jiang, W., Estes, M.K., Prasad, B.V. V., 2009. Rotavirus Architecture at Subnanometer Resolution. *J. Virol.* 83, 1754–1766. <https://doi.org/10.1128/JVI.01855-08>
- Liakopoulou, E., Mutton, K., Carrington, D., Robinson, S., Steward, C.G., Goulden, N.J., Cornish, J.M., Marks, D.I., 2005. Rotavirus as a significant cause of prolonged diarrhoeal illness and morbidity following allogeneic bone marrow transplantation. *Bone Marrow Transplant.* 36, 691–694. <https://doi.org/10.1038/sj.bmt.1705127>
- Livak, K.J., Schmittgen, T.D., 2001. Analysis of relative gene expression data using real-time quantitative PCR and the 2- $\Delta\Delta$ CT method. *Methods* 25, 402–408. <https://doi.org/10.1006/meth.2001.1262>
- Lockwood, H., 2017. Regulation of the Transcriptome of Rotavirus-Infected HT29.f8 cells by Arachidin-3. Stephen F. Austin.
- Long, C.P., McDonald, S.M., 2017. Rotavirus genome replication: Some assembly required. *PLoS Pathog.* 13, 1–6. <https://doi.org/10.1371/journal.ppat.1006242>
- Lopez, T., Camacho, M., Zayas, M., Najera, R., Sanchez, R., Arias, C.F., Lopez, S., 2005. Silencing the Morphogenesis of Rotavirus. *J. Virol.* 79, 184–192. <https://doi.org/10.1128/JVI.79.1.184-192.2005>
- Lu, X., McDonald, S.M., Tortorici, M.A., Tao, Y.J., Carpio, V., Nibert, M.L., Patton, J.T., Harrison, S.C., 2009. Mechanism for coordinated RNA packaging and genome replication by rotavirus polymerase VP1. *Structure* 16, 1678–1688. <https://doi.org/10.1016/j.str.2008.09.006>
- Lu, X., McDonald, S.M., Tortorici, M.A., Tao, Y.J., Vasquez-Del Carpio, R., Nibert, M.L., Patton, J.T., Harrison, S.C., 2008. Mechanism for Coordinated RNA Packaging and Genome Replication by Rotavirus Polymerase VP1. *Structure* 16, 1678–1688. <https://doi.org/10.1016/j.str.2008.09.006>
- Lykidis, A., Wang, J., Karim, M.A., Jackowski, S., 2001. Overexpression of a mammalian ethanolamine-specific kinase accelerates the CDP-ethanolamine pathway. *J. Biol. Chem.* 276, 2174–2179. <https://doi.org/10.1074/jbc.M008794200>

- Matsuda, L.A., Lolait, S.J., Brownstein, M.J., Young, A.C., Bonner, T.I., 1990. Structure of a cannabinoid receptor and functional expression of the cloned cDNA. *Nature* 346, 561–564. <https://doi.org/doi:10.1038/346561a0>
- Mazzon, M., Mercer, J., 2014. Lipid interactions during virus entry and infection. *Cell. Microbiol.* 16, 1493–1502. <https://doi.org/10.1111/cmi.12340>
- McClain, B., Settembre, E., Temple, B.R.S., Bellamy, A.R., Harrison, S.C., 2010. X-Ray crystal structure of the rotavirus inner capsid particle at 3.8 Å resolution. *J Mol Biol.* 397, 587–599. <https://doi.org/10.1016/j.jmb.2010.01.055.X-ray>
- McPartland, J.M., Matias, I., Di Marzo, V., Glass, M., 2006. Evolutionary origins of the endocannabinoid system. *Gene* 370, 64–74. <https://doi.org/https://doi.org/10.1016/j.gene.2005.11.004>
- Mohan, K. V., Muller, J., Atreya, C.D., 2008. Defective rotavirus particle assembly in lovastatin-treated MA104 cells. *Arch. Virol.* 153, 2283–2290. <https://doi.org/10.1007/s00705-008-0261-0>
- Moss, R., Mao, Q., Taylor, D., Saucier, C., 2013. Investigation of monomeric and oligomeric wine stilbenoids in red wines by ultra-high-performance liquid chromatography/electrospray ionization quadrupole time-of-flight mass spectrometry. *Rapid Commun. Mass Spectrom.* 27, 1815–1827. <https://doi.org/10.1002/rcm.6636>
- Munro, S., Thomas, K.L., Abu-Shaar, M., 1993. Molecular characterization of a peripheral receptor for cannabinoids. *Nature* 365, 61–65. <https://doi.org/doi:10.1038/365061a0>
- Mwila-kazimbaya, K., Bosomprah, S., Simuyandi, M., Chisenga, C.C., Munsaka, S., 2018. Efficacy and Effectiveness of Rotavirus Vaccine on Incidence of Diarrhoea among Children : A Meta-analysis. *Pediatr. Infect. Dis.* 3, 1–11. <https://doi.org/10.4172/2573-0282.100060>
- Napier-Jameson, R., 2018. The Comparison of Effects of Synthetic and Natural Arachidin-3 on Rotavirus Infected Cells. Stephen F. Austin State University.
- Pacher, P., Batkai, S., Kunos, G., 2006. The Endocannabinoid System as an Emerging Target of Pharmacotherapy. *Pharmacol Rev.* 58, 213–223. <https://doi.org/10.1007/978-1-62703-673-3>
- Pacher, P., George, K., 2013. Modulating the endocannabinoid system in human health and disease: successes and failures 280, 1918–1943. <https://doi.org/10.1111/febs.12260>
- Patton, J.T., 2009. Rotavirus Diversity and Evolution in the Post-Vaccine World. *Discov Med* 49, 1841–1850.

- Plaza, J.J.G., Hulak, N., Kausova, G., Zhumadilov, Z., Akilzhanova, A., 2016. Role of metabolism during viral infections, and crosstalk with the innate immune system. *Intractable Rare Dis. Res.* 5, 90–96. <https://doi.org/10.5582/irdr.2016.01008>
- Plikaytis, B.D., Sc, M., Makombe, N.S., Mcneal, M.M., Sc, M., Meyer, N., Sc, M., Adehossi, E., Djibo, A., Jochum, B., Grais, R.F., Ph, D., 2017. Efficacy of a Low-Cost, Heat-Stable Oral Rotavirus Vaccine in Niger. *N. Engl. J. Med.* 376, 1121–1130. <https://doi.org/10.1056/NEJMoa1609462>
- Prasad, B. V., Rothnagel, R., Zeng, C.Q., Jakana, J., Lawton, J.A., Chiu, W., Estes, M.K., 1996. Visualization of ordered genomic RNA and localization of transcriptional complexes in rotavirus. *Nature* 382, 471–473. <https://doi.org/10.1038/382471a0>
- Radhakrishnan, A., Ikeda, Y., Kwon, H.J., Brown, M.S., Goldstein, J.L., 2007. Sterol-regulated transport of SREBPs from endoplasmic reticulum to Golgi: Oxysterols block transport by binding to Insig. *Proc. Natl. Acad. Sci.* 104, 6511–6518. <https://doi.org/10.1073/pnas.0700899104>
- Reeskamp, L.F., Meessen, E.C.E., Groen, A.K., 2018. Transintestinal cholesterol excretion in humans. *Curr. Opin. Lipidol.* 29, 10–17. <https://doi.org/10.1097/MOL.0000000000000473>
- Rodriguez De Fonseca, F., Schneider, M., 2008. The endogenous cannabinoid system and drug addiction: 20 Years after the discovery of the CB1 receptor. *Addict. Biol.* 13, 143–146. <https://doi.org/10.1111/j.1369-1600.2008.00116.x>
- Roupe, K., Remsberg, C., Yanez, J., Davies, N., 2006. Pharmacometrics of Stilbenes: Seguing Towards the Clinic. *Curr. Clin. Pharmacol.* 1, 81–101. <https://doi.org/10.2174/157488406775268246>
- Ruiz, M.C., Leon, T., Diaz, Y., Michelangeli, F., 2009. Molecular Biology of Rotavirus Entry and Replication. *Sci. World J.* 9, 1476–1497. <https://doi.org/10.1100/tsw.2009.158>
- Sanchez, E.L., Lagunoff, M., 2015. Viral activation of cellular metabolism. *Virology* 479–480, 609–618. <https://doi.org/10.1016/j.virol.2015.02.038>
- Settembre, E.C., Chen, J.Z., Dormitzer, P.R., Grigorieff, N., Harrison, S.C., 2011. Atomic model of an infectious rotavirus particle. *EMBO J.* 30, 408–416. <https://doi.org/10.1038/emboj.2010.322>
- Sharkey, K.A., Wiley, J.W., 2016. The Role of the Endocannabinoid System in the Brain–Gut Axis. *Gastroenterology* 151, 252–266. <https://doi.org/10.1053/j.gastro.2016.04.015>

- Sharma, C., Sadek, B., Goyal, S.N., Sinha, S., Kamal, M.A., Ojha, S., 2015. Small Molecules from Nature Targeting G-Protein Coupled Cannabinoid Receptors: Potential Leads for Drug Discovery and Development. Evidence-based Complement. Altern. Med. 2015. <https://doi.org/10.1155/2015/238482>
- Silva Afonso, M., Marcondes Machado, R., Ferrari Lavrador, M.S., Rocha Quintao, E.C., Moore, K.J., Lottenberg, A.M., 2018. Molecular pathways underlying cholesterol homeostasis. *Nutrients* 10, 1–18. <https://doi.org/10.3390/nu10060760>
- Silvestri, L., Taraporewala, Z., Patton, J., 2004. Rotavirus Replication : Plus-Sense Templates for Double-Stranded RNA Synthesis Are Made in Viroplasm. *J. Virol.* 78, 7763–7774. <https://doi.org/10.1128/JVI.78.14.7763>
- Sobolev, V.S., 2013. Production of Phytoalexins in Peanut (*Arachis hypogaea*) Seed Elicited by Selected Microorganisms. *J. Agric. Food Chem.* 61, 1850–1858. <https://doi.org/10.1021/jf3054752>
- Spencer, E., Arias, M.L., 1981. In vitro transcription catalyzed by heat-treated human rotavirus. *J. Virol.* 40, 1–10.
- Stelzmueller, I., Wiesmayr, S., Swenson, B.R., Biebl, M., Goegele, H., Margreiter, R., Bonatti, H., 2007. Rotavirus enteritis in solid organ transplant recipients: an underestimated problem? *Transpl. Infect. Dis.* 9, 281–285. <https://doi.org/10.1111/j.1399-3062.2007.00251.x>
- Sugata, K., Taniguchi, K., Yui, A., Nakai, H., Asano, Y., Hashimoto, S., Ihira, M., Yagasaki, H., Takahashi, Y., Kojima, S., Matsumoto, K., Kato, K., Yoshikawa, T., 2012. Analysis of rotavirus antigenemia in hematopoietic stem cell transplant recipients. *Transpl. Infect. Dis.* 14, 49–56. <https://doi.org/10.1111/j.1399-3062.2011.00668.x>
- Sun, Z., Gong, J., Wu, H., Xu, W., Wu, L., Xu, D., Gao, J., Wu, J.W., Yang, H., Yang, M., Li, P., 2013. Perilipin1 promotes unilocular lipid droplet formation through the activation of Fsp27 in adipocytes. *Nat. Commun.* 4, 1514–1594. <https://doi.org/10.1038/ncomms2581>
- Tomé-Carneiro, J., Larrosa, M., González-Sarrías, A., Tomás-Barberán, F., García-Conesa, M., Espín, J., 2013. Resveratrol and Clinical Trials: The Crossroad from In Vitro Studies to Human Evidence. *Curr. Pharm. Des.* 19, 6064–6093. <https://doi.org/10.2174/13816128113199990407>
- Trask, D.S., McDonald, S.M., Patton, J.T., 2012. Structural insights into the coupling of virion assembly and rotavirus replication. *Nat. Rev. Microbiol.* 10, 165–177. <https://doi.org/10.138/nrmicro2673>

- Trautmann, S.M., Sharkey, K.A., 2015. Chapter Three - The Endocannabinoid System and Its Role in Regulating the Intrinsic Neural Circuitry of the Gastrointestinal Tract, in: Parsons, L., Hill, M.B.T.-I.R. of N. (Eds.), *Endocannabinoids*. Academic Press, pp. 85–126. <https://doi.org/https://doi.org/10.1016/bs.irn.2015.10.002>
- Troy-Fioramonti, S., Demizieux, L., Gresti, J., Muller, T., Vergès, B., Degrace, P., 2015. Acute activation of cannabinoid receptors by anandamide reduces gastrointestinal motility and improves postprandial glycemia in mice. *Diabetes* 64, 808–818. <https://doi.org/10.2337/db14-0721>
- Vesikari, T., Matson, D.O., Dennehy, P., Van Damme, P., Santosham, M., Rodriguez, Z., Dallas, M.J., Heyse, J.F., Goveia, M.G., Black, S.B., Shinefield, H.R., Christie, C.D.C., Ylitalo, S., Itzler, R.F., Coia, M.L., Onorato, M.T., Adeyi, B.A., Marshall, G.S., Gothefors, L., Campens, D., Karvonen, A., Watt, J.P., O'Brien, K.L., DiNubile, M.J., Clark, H.F., Boslego, J.W., Offit, P.A., Heaton, P.M., 2006. Safety and Efficacy of a Pentavalent Human–Bovine (WC3) Reassortant Rotavirus Vaccine. *N. Engl. J. Med.* 354, 23–33. <https://doi.org/10.1056/NEJMoa052664>
- Voet, D., Voet, J.G., 2011. Lipid Metabolism, in: *Biochemistry*. John Wiley & Sons, Hoboken, NJ, pp. 961–995.
- Weinberg, G.A., Teel, E.N., Mijatovic-Rustempasic, S., Payne, D.C., Roy, S., Foytich, K., Parashar, U.D., Gentsch, J.R., Bowen, M.D., 2013. Detection of novel rotavirus strain by vaccine postlicensure surveillance. *Emerg. Infect. Dis.* 19, 1321–1323. <https://doi.org/10.3201/eid1908.130470>
- Witcher, C.M., 2017. The Regulation of Rotavirus - Infected HT29.f8 and MA104 Cells Treated with Arachidin 1 or Arachidin 3. *Electron. Theses Diss.* Stephen F. Austin.
- Wright, K., Rooney, N., Feeney, M., Tate, J., Robertson, D., Welham, M., Ward, S., 2005. Differential expression of cannabinoid receptors in the human colon: Cannabinoids promote epithelial wound healing. *Gastroenterology* 129, 437–453. <https://doi.org/10.1016/j.gastro.2005.05.026>
- Wright, K.L., Duncan, M., Sharkey, K.A., 2008. Cannabinoid CB<sub>2</sub> receptors in the gastrointestinal tract: a regulatory system in states of inflammation. *Br. J. Pharmacol.* 153, 263–270. <https://doi.org/10.1038/sj.bjp.0707486>
- Yang, T., Fang, L., Rimando, A.M., Sobolev, V., Mockaitis, K., Medina-Bolivar, F., 2016. Characterization of stilbenoid-specific prenyltransferase activity in peanut hairy roots. *Plant Physiol.* 171, 2483–2498. <https://doi.org/10.1104/pp.16.00610>

- Yen, C., Tate, J.E., Hyde, T.B., Cortese, M.M., Lopman, B.A., Jiang, B., Glass, R.I., Parashar, U.D., 2014. Rotavirus vaccines. *Hum. Vaccin. Immunother.* 10, 1436–1448. <https://doi.org/10.4161/hv.28857>
- Yin, Y., Metselaar, H.J., Sprengers, D., Peppelenbosch, M.P., Pan, Q., 2015. Rotavirus in organ transplantation: Drug-virus-host interactions. *Am. J. Transplant.* 15, 585–593. <https://doi.org/10.1111/ajt.13135>

## APPENDIX

Table 10. cDNA optimization calculations

<b>cDNA processing kit</b>	<b>Unprocessed cDNA concentration (ng/<math>\mu</math>L)</b>	<b>Post-processed cDNA concentration (ng/<math>\mu</math>L)</b>	<b>Percent recovery</b>
Monarch® PCR & DNA Cleanup Kit	<b>825</b>	<b>65.69</b>	<b>7.9%</b>
Zymo One Step PCR Inhibitor Removal	<b>635</b>	<b>45.87</b>	<b>7.2%</b>
Zymo Research DNA Clean & Concentrator™ - 5	<b>605.2</b>	<b>0</b>	<b>0%</b>

Table 11. RT<sup>2</sup> Profiler PCR Array data and calculations (continued)

GENE	NV	$\Delta Ct$	RV	$\Delta Ct$	$\Delta\Delta Ct$	FC	RV+A3	$\Delta Ct$	$\Delta\Delta Ct$	FC	A3	$\Delta Ct$	$\Delta\Delta Ct$	FC
ABCA1	29.420	7.701	30.281	7.316	-0.385	<b>1.306</b>	30.611	8.334	0.634	<b>0.645</b>	30.107	8.446	0.745	<b>0.597</b>
ABCG1	29.590	7.871	32.097	9.133	1.261	<b>0.417</b>	30.990	8.714	0.843	<b>0.558</b>	31.080	9.419	1.548	<b>0.342</b>
ACAA2	24.661	2.942	25.736	2.771	-0.171	<b>1.126</b>	25.272	2.995	0.054	<b>0.964</b>	24.940	3.279	0.337	<b>0.792</b>
AKR1D1	37.412	N/A	0.000				39.817	N/A			38.356			
ANGPLT3	32.638	10.919	32.886	9.921	-0.998	<b>1.997</b>	31.714	9.437	-1.481	<b>2.792</b>	32.208	10.547	-0.372	<b>1.294</b>
ANKRA2	28.530	6.811	29.455	6.490	-0.321	<b>1.250</b>	28.228	5.951	-0.860	<b>1.816</b>	28.060	6.398	-0.413	<b>1.331</b>
APOA1	31.487	9.768	31.988	9.023	-0.745	<b>1.676</b>	31.651	9.375	-0.393	<b>1.313</b>	31.207	9.546	-0.222	<b>1.166</b>
APOA2	32.324	10.605	34.701	11.736	1.131	<b>0.457</b>	33.329	11.053	0.447	<b>0.733</b>	33.408	11.746	1.141	<b>0.453</b>
APOA4	31.682	9.963	32.415	9.450	-0.513	<b>1.427</b>	32.838	10.561	0.598	<b>0.660</b>	29.807	8.146	-1.817	<b>3.524</b>
APOB	35.258	13.539	35.023	12.058	-1.481	<b>2.791</b>	37.193	N/A			37.569			
APOC3	36.800	15.081	38.142				38.425	N/A			38.026			
APOD	32.407	10.688	33.101	10.136	-0.552	<b>1.466</b>	33.442	11.165	0.477	<b>0.718</b>	33.290	11.629	0.941	<b>0.521</b>
APOE	29.813	8.094	30.752	7.787	-0.307	<b>1.237</b>	30.161	7.884	-0.210	<b>1.156</b>	29.414	7.753	-0.341	<b>1.267</b>
APOF	34.090	12.371	34.998	12.033	-0.338	<b>1.264</b>	33.866	11.589	-0.782	<b>1.719</b>	33.330	11.668	-0.702	<b>1.627</b>
APOL1	27.224	5.505	28.609	5.644	0.139	<b>0.908</b>	28.285	6.009	0.503	<b>0.705</b>	27.157	5.496	-0.009	<b>1.006</b>
APOL2	28.975	7.256	29.983	7.019	-0.238	<b>1.179</b>	29.429	7.152	-0.105	<b>1.075</b>	29.277	7.616	0.359	<b>0.780</b>
APOL5	33.336	11.618	35.277				33.900	11.623	0.005	<b>0.996</b>	33.114	11.453	-0.165	<b>1.121</b>
CDH13	35.682	13.963	40.008				39.739	N/A			39.172			
CEL	31.126	9.407	32.813	9.848	0.441	<b>0.737</b>	32.092	9.816	0.408	<b>0.753</b>	31.219	9.558	0.151	<b>0.901</b>
CELA3A	29.068	7.350	29.940	6.975	-0.374	<b>1.296</b>	29.376	7.099	-0.250	<b>1.189</b>	28.265	6.604	-0.746	<b>1.677</b>
CELA3B	31.874	10.155	34.387	11.422	1.267	<b>0.415</b>	33.478	11.201	1.046	<b>0.484</b>	0.000			
CETP	36.757	15.038	39.237				0.000	N/A			32.906	11.245	-3.793	<b>13.858</b>
CNBP	23.225	1.506	24.713	1.748	0.242	<b>0.845</b>	24.283	2.006	0.500	<b>0.707</b>	38.941			
COLEC12	36.192	14.473	39.031				0.000	N/A			23.718	2.057	-12.416	<b>5466.108</b>
CXCL16	28.530	6.811	30.158	7.193	0.382	<b>0.767</b>	29.416	7.139	0.328	<b>0.797</b>	29.135	7.474	0.663	<b>0.631</b>
CYBR3	25.328	3.609	26.983	4.018	0.409	<b>0.753</b>	26.358	4.082	0.473	<b>0.721</b>	25.500	3.839	0.230	<b>0.853</b>
CYP11A1	35.370	13.651	36.115				35.489	N/A			35.871			
CYP39A1	31.281	9.562	31.703	8.738	-0.824	<b>1.770</b>	31.897	9.621	0.058	<b>0.960</b>	31.073	9.412	-0.150	<b>1.110</b>
CYP46A1	31.625	9.907	34.265	11.300	1.393	<b>0.381</b>	33.837	11.560	1.654	<b>0.318</b>	32.951	11.289	1.383	<b>0.383</b>
CYP51A1	23.036	1.317	24.144	1.179	-0.138	<b>1.101</b>	23.404	1.127	-0.190	<b>1.141</b>	23.017	1.356	0.039	<b>0.974</b>
CYP7A1	34.907	13.189	35.292				38.218	N/A			37.639			
CYP7B1	34.535	12.816	0.000				39.907	N/A			37.255			
DHCR24	23.812	2.093	25.692	2.727	0.634	<b>0.644</b>	25.201	2.925	0.832	<b>0.562</b>	24.726	3.065	0.972	<b>0.510</b>
DHCR7	23.975	2.256	25.785	2.821	0.565	<b>0.676</b>	24.971	2.694	0.439	<b>0.738</b>	24.394	2.732	0.476	<b>0.719</b>
FDFT1	23.893	2.174	25.537	2.572	0.398	<b>0.759</b>	24.933	2.656	0.482	<b>0.716</b>	24.256	2.595	0.421	<b>0.747</b>
FDPS	23.840	2.121	25.340	2.375	0.254	<b>0.839</b>	24.613	2.336	0.214	<b>0.862</b>	24.325	2.663	0.542	<b>0.687</b>
HDLBP	24.741	3.022	26.407	3.442	0.420	<b>0.747</b>	26.224	3.947	0.925	<b>0.527</b>	25.585	3.924	0.902	<b>0.535</b>
HMGCR	24.908	3.189	26.062	3.097	-0.091	<b>1.065</b>	25.456	3.180	-0.009	<b>1.006</b>	24.955	3.294	0.105	<b>0.930</b>

Table 11. RT<sup>2</sup> Profiler PCR Array data and calculations (continued)

GENE	NV	$\Delta Ct$	RV	$\Delta Ct$	$\Delta\Delta Ct$	FC	RV+A3	$\Delta Ct$	$\Delta\Delta Ct$	FC	A3	$\Delta Ct$	$\Delta\Delta Ct$	FC
HMGCS1	23.447	1.728	24.535	1.570	-0.158	<b>1.116</b>	24.076	1.799	0.071	<b>0.952</b>	23.634	1.972	0.244	<b>0.844</b>
HMGCS2	24.006	2.287	25.365	2.400	0.114	<b>0.924</b>	25.080	2.803	0.516	<b>0.699</b>	24.572	2.910	0.624	<b>0.649</b>
ID1	24.317	2.598	25.005	2.040	-0.558	<b>1.472</b>	24.087	1.810	-0.788	<b>1.726</b>	23.804	2.143	-0.455	<b>1.371</b>
ID2	31.865	10.146	33.536	10.571	0.425	<b>0.745</b>	32.269	9.992	-0.153	<b>1.112</b>	31.843	10.181	0.036	<b>0.976</b>
IL4	35.878	14.159	35.866				37.159	N/A			34.365	12.703	-1.456	<b>2.743</b>
INSIG1	24.382	2.663	25.291	2.326	-0.337	<b>1.263</b>	24.352	2.076	-0.588	<b>1.503</b>	24.124	2.462	-0.201	<b>1.150</b>
INSIG2	26.479	4.761	27.626	4.661	-0.100	<b>1.072</b>	27.080	4.803	0.043	<b>0.971</b>	26.790	5.128	0.368	<b>0.775</b>
LCAT	30.808	9.089	31.417	8.452	-0.638	<b>1.556</b>	31.616	9.340	0.250	<b>0.841</b>	31.153	9.492	0.402	<b>0.757</b>
LDLR	24.982	3.263	26.294	3.329	0.066	<b>0.955</b>	25.780	3.503	0.240	<b>0.847</b>	25.293	3.632	0.369	<b>0.774</b>
LDLRAP1	29.891	8.172	32.392	9.427	1.254	<b>0.419</b>	30.938	8.661	0.489	<b>0.713</b>	30.541	8.880	0.707	<b>0.612</b>
LEP	31.204	9.486	34.504	11.539	2.053	<b>0.241</b>	33.729	11.452	1.967	<b>0.256</b>	33.357	11.695	2.210	<b>0.216</b>
LIPE	29.610	7.891	30.528	7.563	-0.328	<b>1.255</b>	30.123	7.846	-0.044	<b>1.031</b>	29.430	7.768	-0.122	<b>1.089</b>
LRP10	27.245	5.526	29.029	6.064	0.538	<b>0.689</b>	28.206	5.929	0.403	<b>0.756</b>	27.553	5.892	0.366	<b>0.776</b>
LRP12	29.943	8.224	30.328	7.363	-0.861	<b>1.816</b>	30.571	8.294	0.070	<b>0.953</b>	29.936	8.275	0.051	<b>0.965</b>
LRP1B	35.013	13.294	0.000				0.000	N/A			0.000			
LRP6	26.647	4.928	27.377	4.412	-0.516	<b>1.430</b>	27.039	4.763	-0.166	<b>1.122</b>	27.117	5.456	0.528	<b>0.694</b>
LRPAP1	25.565	3.846	26.646	3.681	-0.165	<b>1.121</b>	26.045	3.769	-0.078	<b>1.055</b>	25.340	3.679	-0.168	<b>1.123</b>
MBTPS1	27.063	5.344	28.064	5.099	-0.245	<b>1.185</b>	27.695	5.419	0.075	<b>0.950</b>	27.128	5.467	0.123	<b>0.918</b>
MVD	28.138	6.419	30.019	7.054	0.634	<b>0.644</b>	28.639	6.362	-0.057	<b>1.040</b>	28.231	6.570	0.151	<b>0.901</b>
MVK	27.862	6.143	29.684	6.719	0.576	<b>0.671</b>	28.896	6.619	0.477	<b>0.719</b>	28.323	6.662	0.519	<b>0.698</b>
NPC1L1	32.037	10.318	36.037				35.102	N/A			35.161			
NR0B2	26.707	4.988	28.453	5.488	0.500	<b>0.707</b>	28.066	5.789	0.801	<b>0.574</b>	27.279	5.618	0.630	<b>0.646</b>
NR1H4	34.452	12.733	35.206				36.620	N/A			34.981	13.320	0.587	<b>0.666</b>
NSDHL	26.366	4.647	27.910	4.945	0.298	<b>0.814</b>	27.613	5.337	0.689	<b>0.620</b>	26.802	5.140	0.493	<b>0.711</b>
OLR1	34.572	12.853	38.206				34.619	12.342	-0.511	<b>1.425</b>	34.299	12.638	-0.215	<b>1.161</b>
OSBPL1A	27.554	5.836	28.456	5.491	-0.344	<b>1.270</b>	28.055	5.778	-0.058	<b>1.041</b>	27.512	5.850	0.015	<b>0.990</b>
OSBPL5	28.330	6.611	30.029	7.064	0.453	<b>0.730</b>	29.388	7.111	0.500	<b>0.707</b>	28.639	6.978	0.367	<b>0.775</b>
FCSK9	28.437	6.719	30.195	7.230	0.511	<b>0.702</b>	28.979	6.702	-0.017	<b>1.012</b>	28.584	6.923	0.204	<b>0.868</b>
PMVK	25.832	4.113	26.971	4.006	-0.107	<b>1.077</b>	26.276	3.999	-0.114	<b>1.082</b>	25.484	3.822	-0.291	<b>1.223</b>
PPARD	28.419	6.700	30.010	7.046	0.345	<b>0.787</b>	29.214	6.937	0.237	<b>0.849</b>	28.703	7.041	0.341	<b>0.790</b>
PRKAA1	24.454	2.735	26.056	3.091	0.356	<b>0.781</b>	25.286	3.010	0.275	<b>0.827</b>	25.005	3.344	0.609	<b>0.656</b>
PRKAA2	34.369	12.650	36.393				35.994	N/A			36.393			
PRKAG2	27.972	6.253	29.045	6.080	-0.173	<b>1.127</b>	28.634	6.357	0.104	<b>0.931</b>	27.950	6.288	0.035	<b>0.976</b>
SCAP	29.993	8.274	31.765	8.800	0.526	<b>0.695</b>	31.308	9.032	0.757	<b>0.592</b>	30.670	9.008	0.734	<b>0.601</b>
SCARF1	32.331	10.612	33.875	10.910	0.297	<b>0.814</b>	34.170	11.893	1.281	<b>0.411</b>	32.561	10.900	0.288	<b>0.819</b>
SNX17	25.282	3.563	26.692	3.727	0.164	<b>0.892</b>	25.687	3.410	-0.153	<b>1.112</b>	25.137	3.476	-0.087	<b>1.062</b>
SOAT1	26.244	4.525	27.558	4.593	0.068	<b>0.954</b>	26.898	4.621	0.097	<b>0.935</b>	26.326	4.664	0.140	<b>0.908</b>
SORL1	26.414	4.696	27.606	4.641	-0.054	<b>1.038</b>	27.894	5.618	0.922	<b>0.528</b>	27.036	5.374	0.679	<b>0.625</b>
SREBF1	27.782	6.063	29.363	6.398	0.335	<b>0.793</b>	28.460	6.183	0.121	<b>0.920</b>	27.976	6.314	0.252	<b>0.840</b>
SREBF2	25.379	3.661	26.781	3.816	0.155	<b>0.898</b>	26.118	3.841	0.181	<b>0.882</b>	25.662	4.001	0.340	<b>0.790</b>

Table 11. RT<sup>2</sup> Profiler PCR Array data and calculations (continued)

GENE	NV	$\Delta Ct$	RV	$\Delta Ct$	$\Delta\Delta Ct$	FC	RV+A3	$\Delta Ct$	$\Delta\Delta Ct$	FC	A3	$\Delta Ct$	$\Delta\Delta Ct$	FC
STAB1	33.130	11.411	33.733	10.768	-0.643	<b>1.562</b>	33.220	10.943	-0.468	<b>1.383</b>	32.419	10.758	-0.653	<b>1.573</b>
STAB2	32.396	10.677	35.483				34.316	12.039	1.362	<b>0.389</b>	32.316	10.654	-0.022	<b>1.016</b>
STARD3	27.527	5.808	30.037	7.072	1.264	<b>0.416</b>	28.768	6.491	0.683	<b>0.623</b>	28.365	6.703	0.895	<b>0.538</b>
TM7SF2	26.121	4.402	27.865	4.900	0.499	<b>0.708</b>	27.420	5.143	0.741	<b>0.598</b>	26.484	4.823	0.421	<b>0.747</b>
TRERF1	29.020	7.301	30.937	7.972	0.670	<b>0.628</b>	30.212	7.935	0.634	<b>0.645</b>	29.952	8.291	0.990	<b>0.504</b>
VLDLR	31.611	9.892	33.813	10.848	0.957	<b>0.515</b>	33.097	10.820	0.928	<b>0.526</b>	33.284	11.622	1.731	<b>0.301</b>
ACTB	19.332		21.013				20.876				20.077			
B2M	<b>22.437</b>		<b>23.325</b>				<b>22.399</b>				<b>21.976</b>			
GAPDH	<b>21.001</b>		<b>22.605</b>				<b>22.155</b>				<b>21.346</b>			
HPRT	26.801		27.656				26.717				26.239			
RPLP0	18.053		19.157				18.300				17.765			
HGDC	38.394		40.382				38.331				39.000			
RTC	21.805		21.264				21.177				21.099			
RTC	21.784		21.216				21.252				21.112			
RTC	21.593		21.592				21.549				21.438			
PPC	19.799		19.823				19.906				19.684			
PPC	19.658		19.721				19.779				19.636			
PPC	19.862		19.857				19.991				19.608			

## VITA

Stormey Wisdom graduated from Louisiana State University – Shreveport with a Bachelors in Biochemistry in May 2017. She entered graduate school at Stephen F. Austin State University, Nacogdoches, Texas in August 2017 and will receive a Master of Science degree in Biotechnology in August 2019.

Permanent Address: 802 N Montgomery St.

Gilmer, TX 75644

Email Address: [sbriana.wisdom@yahoo.com](mailto:sbriana.wisdom@yahoo.com)

Style: Virology

This thesis was typed by Stormey Wisdom.